

Massive MIMO for Communications With Drone Swarms

Prabhu Chandhar, Danyo Danev and Erik G Larsson

The self-archived postprint version of this journal article is available at Linköping University Institutional Repository (DiVA):

<http://urn.kb.se/resolve?urn=urn:nbn:se:liu:diva-147124>

N.B.: When citing this work, cite the original publication.

Chandhar, P., Danev, D., Larsson, E. G. (2018), Massive MIMO for Communications With Drone Swarms, *IEEE Transactions on Wireless Communications*, 17(3), 1604-1629.

<https://doi.org/10.1109/TWC.2017.2782690>

Original publication available at:

<https://doi.org/10.1109/TWC.2017.2782690>

Copyright: Institute of Electrical and Electronics Engineers (IEEE)

<http://www.ieee.org/index.html>

©2018 IEEE. Personal use of this material is permitted. However, permission to reprint/republish this material for advertising or promotional purposes or for creating new collective works for resale or redistribution to servers or lists, or to reuse any copyrighted component of this work in other works must be obtained from the IEEE.



Massive MIMO for Communications with Drone Swarms

Prabhu Chandhar, *Member, IEEE*, Danyo Danev, *Member, IEEE*, and Erik G. Larsson, *Fellow, IEEE*

Abstract—We illustrate the potential of Massive MIMO for communication with unmanned aerial vehicles (UAVs). We consider a scenario where multiple single-antenna UAVs simultaneously communicate with a ground station (GS) equipped with a large number of antennas. Specifically, we discuss the achievable uplink (UAV to GS) capacity performance in the case of line-of-sight (LoS) conditions. We develop a realistic geometric model which incorporates an arbitrary orientation of the GS and UAV antenna elements to characterize the polarization mismatch loss which occurs due to the movement and orientation of the UAVs. A closed-form expression for a lower bound on the ergodic rate for a maximum-ratio combining receiver with estimated channel state information is derived. The optimal antenna spacing that maximizes the ergodic rate achieved by an UAV is also determined for uniform linear and rectangular arrays. It is shown that when the UAVs are spherically uniformly distributed around the GS, the ergodic rate per UAV is maximized for an antenna spacing equal to an integer multiple of one-half wavelength.

Index Terms—unmanned aerial vehicles, Massive MIMO, ergodic capacity

I. INTRODUCTION

In recent years, the use of unmanned aerial vehicles (UAVs), also known as drones, for both civilian and military applications is increasing worldwide. There are different types of UAVs, with varying sizes and capabilities that are used in multitude applications. Depending on the power source, their connectivity range varies from a few meters to several kilometers and their flight time varies from a few minutes to tens of hours. For a comprehensive survey of different type of UAVs, their capabilities, and issues related to communication, readers are referred to [3]–[6] and references therein. The communication between a ground station (GS) and the UAVs involves many challenges. First, UAVs are often equipped with cameras that deliver high-resolution images and videos to the GS, requiring high-speed communication in the ranges of tens of Mbps [3]. The main challenge here is to maintain reliable communication as the link conditions are affected by variations in signal propagation due to the movement of the UAVs in three-dimensional (3D) space. Particularly, the antenna characteristics (radiation pattern and polarization) and orientation can have strong impact on the link performance [5], [7], [8]. Second, many applications also require that the information should be delivered with low latency, down to the

The authors are with the Division of Communication Systems, Dept. of Electrical Engineering (ISY), Linköping University, Sweden (email: {prabhu.c, danyo.danev, erik.g.larsson}@liu.se). Portions of this work were presented at ICUAS 2016 [1] and at IEEE SPAWC 2016 [2].

This work was funded in part by the Swedish Research Council (VR) and ELLIIT.

order of 10 milliseconds [9]. Third, power consumption may be a limitation for certain UAV networks.

Currently, existing wireless technologies, such as Wireless Fidelity (WiFi), ZigBee, and XBee-Pro are being used for communication with UAVs. Since these technologies were originally designed for provision of wireless access in indoor scenarios, their use is limited to very short range, low throughput, and low-mobility applications. Experimental studies have shown that under line-of-sight (LoS) conditions, IEEE 802.11n can provide single link data rates of 10 Mbps up to 500 m (mobility: 5 m/s, latency: 100s of ms) and XBee-Pro can provide 250 Kbps up to a 1 km range [6], [10]. These technologies cannot be used for long-range, high-throughput, high-mobility UAV applications, where the flying speed is in the order of 20–50 m/s [3], [7]. Moreover, these technologies are not suitable for applications where a swarm of UAVs needs simultaneous high-throughput communication with the GS. Consider, for example, 20–30 UAVs streaming high-resolution videos to the GS, each UAV requiring tens of Mbps data rate. Some of the potential applications that require such high-throughput link include border surveillance, crowd management, crop monitoring, 3D cartography, and search and rescue missions after natural disasters such as earthquakes and massive flooding. The list of civilian and military applications for UAV swarms keeps growing [3], [6], [11], [12]. Therefore, a new breakthrough technology is required in order to support UAV applications that need reliable long-range connectivity, high throughput, low power consumption, and low latency.

Massive multiple input multiple output (MIMO) is an emerging technique for 5G cellular wireless access [13]–[15]. It is characterized by its scalability and potential to deliver very high and stable throughputs. In a massive MIMO cellular system, base stations equipped with a very large number of antennas simultaneously serve multiple single-antenna terminals. By coherent closed-loop beamforming, the power is focused into a small region of space, thus reducing interference. It also provides significant improvement in energy efficiency and reduced latency. To avoid channel state information feedback, Massive MIMO uses time-division multiplexing (TDD), exploiting channel reciprocity. In this paper, we argue that a solution for communication with UAV swarms based on Massive MIMO can offer orders of magnitude higher sum-throughput and reliability compared to the direct use of existing standards.

A. Contributions

We consider an uplink communication scenario with LoS and no multipath. In this setup, multiple single-antenna UAVs

simultaneously communicate with a GS which is equipped with an uniform rectangular array (URA). We develop a geometric model which captures the polarization characteristics of the GS and the UAV antennas. Using this model, we answer the following questions:

- What is the achievable uplink capacity per UAV, when a swarm of single antenna UAVs simultaneously communicate with a GS equipped with a large number of antennas?
- What is the optimal antenna spacing in the GS antenna array?
- How does the antenna configuration (i.e. antenna orientation and polarization) at the GS and the UAV affect the link reliability, and what is the appropriate antenna polarization that should be used in order to maintain a reliable communication link?

The performance gain of Massive MIMO is achieved by the orthogonality between the spatial signatures (channel response vectors) of the terminals [13]. Unlike in Rayleigh fading channels, in LoS propagation conditions, the spatial signatures are determined by the position of the terminals. Hence in the UAV application, the interference power is determined by the spatial correlation between the spatial signatures of the different UAVs. This interference power will be continuously changing as the positions of the UAVs change when the UAVs move. For example, in micro UAV networks [5], the UAVs typically move at high speed (10 m/s to 30 m/s) in random directions. Even if the UAVs move along a deterministic trajectory, the interference power will fluctuate due to varying elevation and azimuth angles. Once can then expect multiple independent realizations of the interference power within a short period of time (i.e. in a few milliseconds). Effectively, the UAVs then experience many possible interference realizations within the transmission duration of a codeword. This fact motivates us to analyze the ergodic capacity by averaging over all possible positions of the UAVs. For analytical tractability we assume inverse-SNR power control, leading to max-min fairness in terms of received power. First, we derive a closed-form lower bound on the achievable uplink rate for a maximum-ratio combining (MRC) receiver with estimated channel state information (CSI). Then, we analyze the optimal GS antenna geometry that maximizes the ergodic rate. To the best of our knowledge, this analysis is entirely novel and very different, quantitatively and qualitatively, from the analysis in cellular communications and Rayleigh fading [13]. We also study the ergodic rate performance for the zero-forcing (ZF) receiver with perfect CSI.

We consider that the elements of the GS antenna array as well as the UAV antenna are composed of two orthogonally crossed dipoles. The advantage of a cross-dipole antenna is its quasi-isotropic antenna pattern, and it can be used to transmit and receive electromagnetic waves with different polarizations (linear, circular, and elliptical). We develop an analytically tractable polarization loss model to characterize the channel between the cross-dipole antenna elements at the GS and at the UAV. This model could, in principle, at some effort, be extended to the case of a tripole antennas, which have a closer

to isotropic antenna pattern compared to dipoles. However, we show that in the Massive MIMO setup, the use of cross-dipole antennas is sufficient to obtain very good performance (in terms of rates and reliability) of the communication link, by appropriately orienting the elements of the GS array. The reason is the “polarization diversity” effect that arises when the array comprises many antennas with different orientations.

The proposed Massive MIMO based communication framework could be used for wide range of altitudes and different types of UAVs. In this paper, we interchangably use the terms drone and UAV.

B. Related Works

MIMO for UAV communications: A simulation-based study of multi-user MIMO communications for air traffic management for airplanes flying at altitudes ranging from 5 km to 10 km was presented in [16]. The authors studied the impact of antenna spacing on the sum-capacity performance in the uplink. However, they neither used a detailed geometric model nor studied the impact of the number of antennas on the achievable capacity. MIMO for point-to-point aerial communication was studied in [17]–[19]. The authors used small numbers of antennas (2×2 and 4×4) which is different from Massive MIMO where a very large antenna array (with hundreds or thousands of elements) serve many single antenna terminals. Further, they did not study the impact of polarization mismatch losses due to fluctuations of the UAV antenna orientations.

MIMO performance in LoS conditions: The impact of antenna spacing on the capacity of fixed point-to-point MIMO (20×20) in LoS channels was studied in [20]–[22]. It was shown in [13, Ch. 7] that in two-dimensional (2D) Massive MIMO systems, the LoS channels are asymptotically orthogonal as the number of antennas increases. The impact of different array geometries on the asymptotic channel orthogonality in Massive MIMO systems was studied in [23]. The author showed that in LoS channels, asymptotic orthogonality holds for uniform linear arrays and uniform planar arrays, but not for uniform circular arrays. In [24], the authors showed that in 2D LoS channels, the mainlobe distribution of the interference can be approximated as a Beta-mixture. Assuming that perfect CSI is available, a sum-rate analysis for LoS Massive MIMO systems with different array configurations was studied in [25]. The performance of Massive MIMO in LoS conditions with max-min fairness signal-to-interference-plus-noise ratio (SINR) power control was studied in [26]. However, the authors did not consider ergodic rate performance. All the above mentioned works [23]–[25] considered a fixed half-wavelength antenna spacing and did not consider polarization mismatch losses. Moreover, the above-mentioned works assume that perfect CSI is available at the BS and did not consider mobility of the terminals in their analysis. In contrast, we derive a lower bound on the uplink ergodic rate with estimated CSI, and optimize the antenna array geometry. Our analysis also takes into account the (pseudo-)random orientations of the UAV antennas.

Polarization modeling: A 3D polarization model for MIMO channels with linearly polarized antennas in cellular environ-

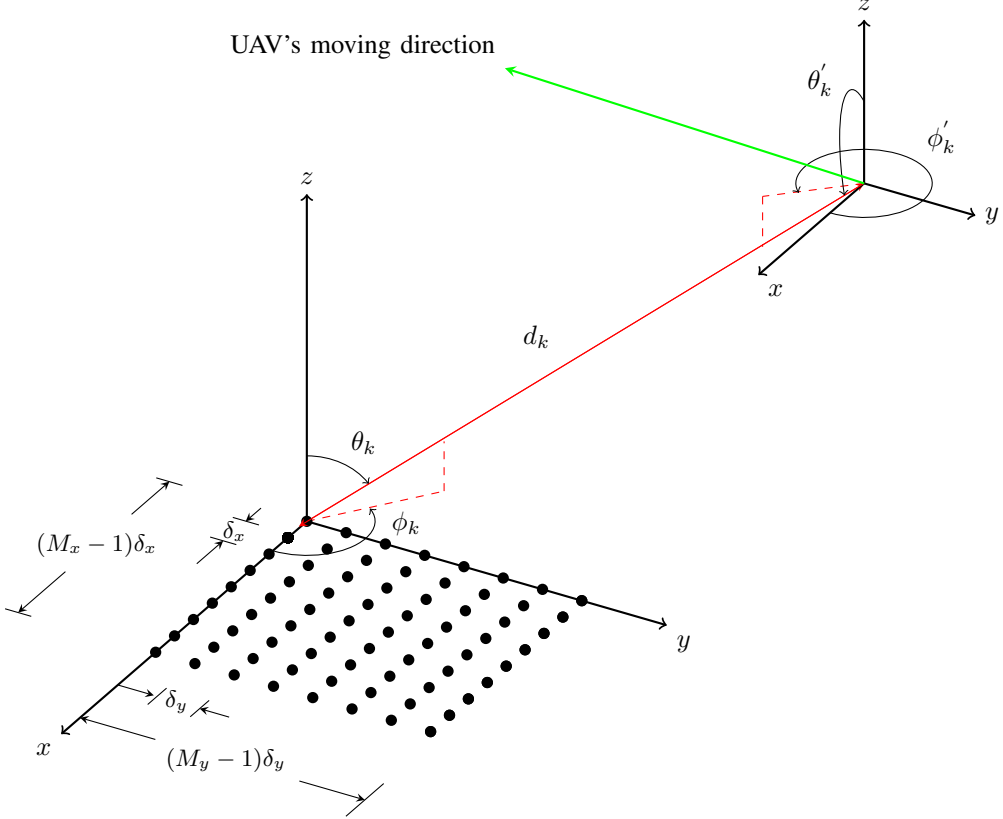


Fig. 1. Illustration of 3D geometric model with a rectangular array at the GS.

ments was developed in [27]. In [28], the authors developed a 3D polarization channel model for a 2×2 MIMO configuration in cellular environments with vertical (V) and horizontal (H) polarizations (i.e., V/V, V/H, and $\pm 45^\circ$ slanted). However, these models cannot be used for UAV communications as the propagation conditions are different from cellular communications¹. A 3D polarization rotation model for both LoS and NLoS conditions was developed in [29]. The authors used a sequence of complicated coordinate system transformations to find the elements of the polarization rotation matrix. An experimental study of IEEE 802.11 networks with 3D mobility was studied in [7]. It was shown that 5 dB to 15 dB gains in received signal strength is possible using three linearly polarized dipole antennas. The authors analyzed the impact of azimuth and elevation angles but they did not analyze the impact of antenna orientations due to flight dynamics (pitch, yaw, roll). In this work, we develop a simpler method, using rotation matrices for the GS and the UAV antennas to incorporate azimuth, elevation, and flight dynamics.

II. SYSTEM MODEL

A. Geometric Model

We consider an uplink of a Massive MIMO system, with LoS and no multipath. The geometric model of the system is

¹The effect of polarization mismatch is not a major problem in cellular communications, because irrespective of the type of transmit antenna polarization, the large number of multipath components (MPCs) arriving at the receive antenna will comprise a combination of all polarizations.

shown in Figure 1. We fix an orthonormal coordinate system with unit basis vectors \hat{x} , \hat{y} , and \hat{z} and an origin at some point O . We refer to this system as a “reference coordinate system”. We consider a rectangular antenna array with M_x and M_y antennas on x -axis and y -axis, respectively. The total number of antenna elements is denoted by $M = M_x M_y$. The spacing between the antenna elements on x -axis and y -axis is denoted by δ_x and δ_y , respectively. The array elements are described by index $l = (q-1)M_x + p$, where $p \in \{1, 2, \dots, M_x\}$ denotes the index on x -axis and $q \in \{1, 2, \dots, M_y\}$ denotes the index on y -axis. The l -th antenna position P^l is denoted by $(x^l, y^l, z^l) = ((p-1)\delta_x, (q-1)\delta_y, 0)$.

There are K single-antenna UAVs simultaneously transmitting data to the GS in the same time-frequency resource. Let the position P_k of the k -th UAV has the coordinates (x_k, y_k, z_k) . The direction vector \mathbf{p}_k from the origin O towards the k -th UAV at position P_k can be expressed as

$$\begin{aligned} \overrightarrow{OP_k} = \mathbf{p}_k &= (\hat{x} \quad \hat{y} \quad \hat{z}) \begin{pmatrix} x_k \\ y_k \\ z_k \end{pmatrix} \\ &= (\hat{x} \quad \hat{y} \quad \hat{z}) \begin{pmatrix} d_k \cos \phi_k \sin \theta_k \\ d_k \sin \phi_k \sin \theta_k \\ d_k \cos \theta_k \end{pmatrix}, \end{aligned}$$

where d_k is the radial distance between the GS and the k -th UAV, $\phi_k \in [0, 2\pi]$ is the azimuth angle (i.e. the angle from the positive direction of the x -axis towards the positive y -axis, to the vector’s (i.e. \mathbf{p}_k ’s) orthogonal projection onto the x - y plane), and $\theta_k \in [0, \pi]$ is the elevation angle (i.e. the angle

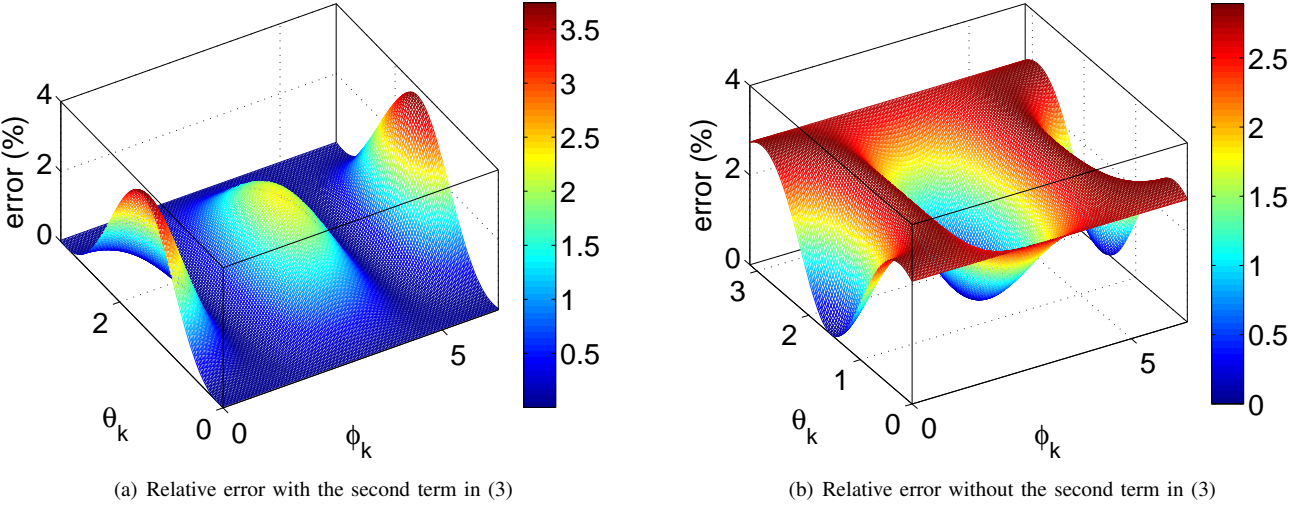


Fig. 2. The approximation error in (3) as a function of the elevation and azimuth angles for $M_x = 100$, $M_y = 1$, $d_k = 25$ m, and $\delta_x = 6.25$ cm.

from the positive direction of the z -axis towards the direction vector \mathbf{p}_k .

The distance between the l -th GS antenna and the k -th UAV's antenna is then given by

$$d_{kl} = \sqrt{(x_k - (p-1)\delta_x)^2 + (y_k - (q-1)\delta_y)^2 + z_k^2}. \quad (1)$$

By expanding (1), we get

$$\begin{aligned} d_{kl} &= d_k \left[1 + \frac{1}{d_k^2} [(p-1)^2 \delta_x^2 + (q-1)^2 \delta_y^2] \right. \\ &\quad \left. - \frac{2}{d_k} \sin \theta_k [(p-1)\delta_x \cos \phi_k + (q-1)\delta_y \sin \phi_k] \right]^{\frac{1}{2}}. \end{aligned} \quad (2)$$

When the distance between the GS antenna and the UAV position is greater than the aperture size of the array i.e. $d_k > \sqrt{(M_x - 1)^2 \delta_x^2 + (M_y - 1)^2 \delta_y^2}$, by using the approximation $\sqrt{1+t} \approx 1 + \frac{t}{2}$, for $|t| < 1$, the distance in (2) can be simplified to

$$\begin{aligned} d_{kl} &\approx d_k + \frac{1}{2d_k} [(p-1)^2 \delta_x^2 + (q-1)^2 \delta_y^2] \\ &\quad - \sin \theta_k [(p-1)\delta_x \cos \phi_k + (q-1)\delta_y \sin \phi_k]. \end{aligned} \quad (3)$$

Note that in our previous works [1], [2], by assuming d_k to be very large when compared to the aperture size, we neglected the second term in (3). However, since the micro UAVs typically fly at very low altitudes in the range from 30 m to 200 m, the distance d_k can be comparable to the aperture size. In this case, the second term in (3) should not be neglected as it will introduce expressive errors in the analysis. For example, Figure 2 shows the error (in %) with and without including the term $\frac{1}{2d_k} ((p-1)^2 \delta_x^2 + (q-1)^2 \delta_y^2)$ for $M_x = 100$, $M_y = 1$, $\delta_x = 6.25$ cm, and $d_k = 25$ m. It can be seen that without the term, the error is significant for most of the elevation and azimuth angles. In contrast, with including the term, the error is small for most of the elevation and azimuth angles. Therefore, in this work, we include the second term in (3) in our analysis.

B. Polarization model with single cross-dipole antenna at the transmitter and the receiver

Let us assume that the l -th GS antenna transmits the signal

$$u(t) = \cos(2\pi f_0 t) = \Re\{e^{i2\pi f_0 t}\},$$

where \Re denotes the real part. In practice, this signal can be realized by creating an alternating electrical current of unit amplitude and frequency f_0 in the transmitter's electrical circuit. The actual transmission takes place when we apply electrical current at the transmit antenna. In our model we consider amplification and phase shifting of the original signal $u(t)$ before applying it to the antenna. The signal's wavelength is $\lambda = c/f_0$, where $c \approx 3 \times 10^8$ m/s is the speed of light.

If the position and the orientation of the k -th UAV is fixed, the signal at its receiver can be expressed as

$$\begin{aligned} v(t) &= \Re \left\{ \sqrt{\beta_{kl}} h_{kl}(f_0) e^{-i \frac{2\pi f_0}{c} d_{kl}} u(t) \right\} \\ &= \sqrt{\beta_{kl}} |h_{kl}(f_0)| \cos \left(2\pi f_0 \left(t - \frac{d_{kl}}{c} \right) + \arg(h_{kl}(f_0)) \right), \end{aligned} \quad (4)$$

where $\beta_{kl} = \left(\frac{\lambda}{4\pi d_{kl}} \right)^2$ is the free-space pathloss [30, Sec: 2.17.1] and the complex number $h_{kl}(f_0)$ represents the combined effect of polarization mismatch and antenna gain. In this subsection we detail the calculation of the factor $h_{kl}(f_0)$ for l -th GS antenna at the UAV.

We fix a translated coordinate system parallel to the reference coordinate system with origin at the l -th GS antenna's position P^l , i.e. (x^l, y^l, z^l) . For the first GS antenna, we get exactly the reference coordinate system. The position P_{kl} of the k -th UAV in the translated coordinate system has coordinates $(x_{kl}, y_{kl}, z_{kl}) = (x_k - (p-1)\delta_x, y_k - (q-1)\delta_y, z_k)$. Each element of the GS array is composed of two orthogonally crossed dipoles (one dipole is oriented parallel to the z -axis and the other to the y -axis). As it will be detailed later, the crossed dipoles are fed with the same signal but with different magnitude and phase. The UAV antenna is also composed of two crossed dipoles oriented along the y - and z -axes (refer

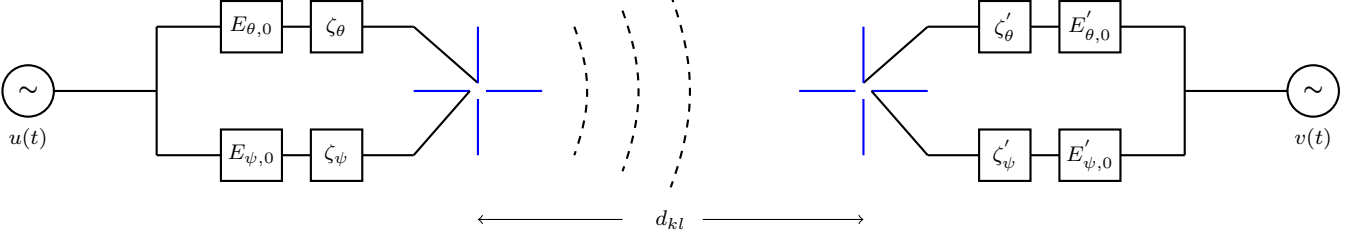


Fig. 3. Communication channel model with crossed dipoles at the transmitter and at the receiver.

Figure 3). Here we consider the downlink communication from the l -th GS antenna to the k -th UAV. For the uplink communication the results are similar due to the antenna reciprocity principle.

Polarization of the wave transmitted by the dipole placed along the z -axis: Polarization of the electromagnetic wave is usually described by the direction of the transmitted wave's electric field vector over time at a given point. The orientation of the electric field is always in the plane orthogonal to the direction of wave propagation. For the dipole placed along the z -axis, the wave travels in the direction towards the k -th UAV

$$\begin{aligned} \overrightarrow{P^l P_k} = \mathbf{p}_{kl} &= (\hat{x} \quad \hat{y} \quad \hat{z}) \begin{pmatrix} x_{kl} \\ y_{kl} \\ z_{kl} \end{pmatrix} \\ &= (\hat{x} \quad \hat{y} \quad \hat{z}) \begin{pmatrix} x_k - (p-1)\delta_x \\ y_k - (q-1)\delta_y \\ z_k \end{pmatrix}. \end{aligned}$$

We denote by $\hat{\mathbf{p}}_{kl} = \frac{\mathbf{p}_{kl}}{\|\mathbf{p}_{kl}\|} = \frac{\mathbf{p}_{kl}}{d_{kl}}$ the unit vector in the direction of the radio wave propagation. The induced electric field will be oriented in the direction of the vector orthogonal to both $\hat{\mathbf{p}}_{kl}$ and $\hat{z} \times \hat{\mathbf{p}}_{kl}$ [30]. The unit length vector determining this direction and having non-negative scalar product with \hat{z} is

$$\hat{\theta}_{kl} = \frac{(\hat{x} \quad \hat{y} \quad \hat{z})}{d_{kl} \sqrt{x_{kl}^2 + y_{kl}^2}} \begin{pmatrix} -x_{kl} z_{kl} \\ -y_{kl} z_{kl} \\ x_{kl}^2 + y_{kl}^2 \end{pmatrix}. \quad (5)$$

The elevation angle between the z -axis directed dipole and the propagation direction is given by

$$\theta_{kl} = \cos^{-1}(\hat{\mathbf{p}}_{kl} \cdot \hat{z}) = \cos^{-1}\left(\frac{z_{kl}}{d_{kl}}\right).$$

Then, for a plane wave propagating in the direction $\hat{\mathbf{p}}_{kl}$, by neglecting the distance factor and phase shift due to propagation delay, the electrical field solution of the wave equation at the direction of the receiver can be expressed in a simplified form as [30]

$$\mathbf{E}_\theta^l(f_0, t) = \hat{\theta}_{kl} \Re \left\{ E_\theta^l F_\theta^l(\theta_{kl}, f_0) e^{i2\pi f_0 t} \right\}. \quad (6)$$

In (6), E_θ^l is a complex scalar, i.e. $E_\theta^l = E_{\theta,0}^l e^{i\zeta_\theta^l}$, where $E_{\theta,0}^l$ is the amplitude and ζ_θ^l is the phase delay of the signal fed to the dipole along the z -axis. The function $F_\theta^l(\theta, f)$ gives the field pattern for the elevation angle θ and the frequency f_0 . If d_{len} is the length of a dipole, the normalized field pattern

(to have a unity maximum gain) of this dipole is given by the function [30, Sec: 4.52]

$$\begin{aligned} F(\theta, f_0) &= \frac{\cos\left(\frac{\pi d_{\text{len}}}{\lambda} \cos \theta\right) - \cos\left(\frac{\pi d_{\text{len}}}{\lambda}\right)}{\sin \theta} \\ &= \frac{\cos\left(\pi f_0 \cos \theta \frac{d_{\text{len}}}{c}\right) - \cos\left(\pi f_0 \frac{d_{\text{len}}}{c}\right)}{\sin \theta}. \end{aligned} \quad (7)$$

It can be observed from (7) that the dipole antenna has an omni-directional radiation pattern only in the azimuth direction but not in elevation. Further, in order to achieve maximum signal reception, the receiving antenna should be aligned along the direction of the incoming wave $\hat{\theta}_{kl}$. If the receiving antenna is aligned along the direction orthogonal to $\hat{\theta}_{kl}$, due to polarization mismatch the received signal strength will be very low. Therefore, we consider another dipole oriented along the y -axis to compensate for it². The total electric field received at a distant point is the superposition of the field components emitted from the dipole antennas oriented along the y - and z -axes.

Polarization of the wave transmitted by the dipole placed along the y -axis: Let $\psi_{kl} = \cos^{-1}(\hat{y} \cdot \hat{\mathbf{p}}_{kl}) = \cos^{-1}\left(\frac{y_{kl}}{d_{kl}}\right)$ be the elevation angle between the dipole oriented along the y -axis and the propagation direction. Then, similarly to (6), the electric field component emitted by the y -axis directed dipole at the direction of the receiver is

$$\mathbf{E}_\psi^l(f_0, t) = \hat{\psi}_{kl} \Re \left\{ E_\psi^l F_\psi^l(\psi_{kl}, f_0) e^{i2\pi f_0 t} \right\},$$

where $E_\psi^l = E_{\psi,0}^l e^{i\zeta_\psi^l}$. The unit direction vector $\hat{\psi}_{kl}$ represents the orientation of the electric field emitted by the y -axis directed dipole. It is in the direction of the vector orthogonal to both $\hat{\mathbf{p}}_{kl}$ and $\hat{y} \times \hat{\mathbf{p}}_{kl}$, i.e.

$$\hat{\psi}_{kl} = \frac{(\hat{x} \quad \hat{y} \quad \hat{z})}{d_{kl} \sqrt{x_{kl}^2 + z_{kl}^2}} \begin{pmatrix} -x_{kl} y_{kl} \\ x_{kl}^2 + z_{kl}^2 \\ -y_{kl} z_{kl} \end{pmatrix}. \quad (8)$$

Polarization of the wave transmitted by the cross-dipole: The total electric field at position P_{kl} is

$$\begin{aligned} \mathbf{E}_{\text{Tot}}^l(f_0, t) &= \mathbf{E}_\theta^l(f_0, t) + \mathbf{E}_\psi^l(f_0, t) \\ &= \Re \left\{ \left(\hat{\theta}_{kl} E_\theta^l F_\theta^l(\theta_{kl}, f_0) + \hat{\psi}_{kl} E_\psi^l F_\psi^l(\psi_{kl}, f_0) \right) e^{i2\pi f_0 t} \right\}. \end{aligned} \quad (9)$$

At various time instances, the orientation of the electric field will be in the $\hat{\theta}_{kl} - \hat{\psi}_{kl}$ plane which is orthogonal to the

²By placing third dipole along the x -axis, one can achieve a radiation pattern that is even closer to an ideal, isotropic antenna pattern. Further, the polarization mismatch loss also can be significantly reduced.

wave travel direction³. Let the vector function $\mathbf{E}^l(\theta_{kl}, \psi_{kl}, f_0)$ be defined as

$$\mathbf{E}^l(\theta_{kl}, \psi_{kl}, f_0) = \begin{pmatrix} E_\theta^l F_\theta^l(\theta_{kl}, f_0) \\ E_\psi^l F_\psi^l(\psi_{kl}, f_0) \end{pmatrix}. \quad (10)$$

The total electric field vector in (9) can be rewritten as $\mathbf{E}_{\text{Tot}}^l(P_{kl}, f_0, t) = \Re\{\mathcal{E}_l e^{i2\pi f_0 t}\}$, where \mathcal{E}_l is the response vector of the transmit antenna defined as

$$\begin{aligned} \mathcal{E}_{kl} &= (\hat{\theta}_{kl} \hat{\psi}_{kl}) \cdot \mathbf{E}^l(\theta_{kl}, \psi_{kl}, f_0) \\ &= \hat{\theta}_{kl} E_\theta^l(\theta_{kl}, f_0) + \hat{\psi}_{kl} E_\psi^l(\psi_{kl}, f_0). \end{aligned} \quad (11)$$

The polarization of the electric field can be expressed by the unit vector $\hat{\mathcal{E}}_l = \frac{\mathcal{E}_l}{\|\mathcal{E}_l\|}$.

Polarization of the receive cross-dipole: Let $\hat{\mathbf{p}}_{kl}'$ be the propagation direction unit vector measured from the receiver, i.e. $\hat{\mathbf{p}}_{kl} = -\hat{\mathbf{p}}_{kl}'$. When the transmitted electromagnetic wave is illuminated on the antenna at the receiver side, the induced field strength depends on the field patterns of the receive dipoles in the incoming propagation direction. The elevation angles for the receive dipoles oriented along the z - and y -axes are obtained as $\theta'_{kl} = \cos^{-1}(\hat{\mathbf{z}} \cdot \hat{\mathbf{p}}_{kl}') = \cos^{-1}\left(-\frac{z_{kl}}{d_{kl}}\right) = \pi - \theta_{kl}$ and $\psi'_{kl} = \cos^{-1}(\hat{\mathbf{y}} \cdot \hat{\mathbf{p}}_{kl}') = \cos^{-1}\left(-\frac{y_{kl}}{d_{kl}}\right) = \pi - \psi_{kl}$, respectively. Let $F_\theta'^k(\theta'_{kl}, f)$ and $F_\psi'^k(\psi'_{kl}, f)$ be the field patterns of z and y directed receiving dipoles, respectively. The outputs from the dipoles are appropriately amplified and phase shifted in order to match with the polarization of the wave. Let the complex magnitudes of these amplifications be $E_\theta'^k = E_{\theta,0}^l e^{i\zeta_\theta'^k}$ and $E_\psi'^k = E_{\psi,0}^l e^{i\zeta_\psi'^k}$. Similarly to (10), we can define

$$\mathbf{E}'^k(\theta'_{kl}, \psi'_{kl}, f_0) = \begin{pmatrix} E_\theta'^k F_\theta'^k(\theta'_{kl}, f_0) \\ E_\psi'^k F_\psi'^k(\psi'_{kl}, f_0) \end{pmatrix} \quad (12)$$

and the response vector of the receive antenna can be written as

$$\begin{aligned} \mathcal{E}'_{kl} &= (\hat{\mathbf{z}} \hat{\mathbf{y}}) \cdot \mathbf{E}'^k(\theta'_{kl}, \psi'_{kl}, f_0) \\ &= \hat{\mathbf{z}} E_\theta'^k F_\theta'^k(\theta'_{kl}, f_0) + \hat{\mathbf{y}} E_\psi'^k F_\psi'^k(\psi'_{kl}, f_0). \end{aligned} \quad (13)$$

The polarization of the electric field of the receive antenna can be expressed as $\hat{\mathcal{E}}'_k = \frac{\mathcal{E}'_k}{\|\mathcal{E}'_k\|}$.

Polarization loss factor (PLF): The quantity $h_{kl}(f_0)$ in (4) can be obtained by projecting the incident electric field vector (\mathcal{E}_{kl} as given in (11)) upon the receiving antenna response vector (\mathcal{E}'_{kl} as given in (13)), i.e.

$$\begin{aligned} h_{kl}(f_0) &= \mathcal{E}_{kl} \cdot \mathcal{E}'_{kl} = \mathcal{E}_{kl}^H \mathcal{E}'_{kl} \\ &= \left(\mathbf{E}^l(\theta_{kl}, \psi_{kl}, f_0) \right)^H \begin{pmatrix} \hat{\theta}_{kl}^T \\ \hat{\psi}_{kl}^T \end{pmatrix} (\hat{\mathbf{z}} \hat{\mathbf{y}}) \mathbf{E}'^k(\theta'_{kl}, \psi'_{kl}, f_0) \\ &= \left(\mathbf{E}^l(\theta_{kl}, \psi_{kl}, f_0) \right)^H \mathbf{T}_{kl} \mathbf{E}'^k(\theta'_{kl}, \psi'_{kl}, f_0). \end{aligned}$$

³The polarization (i.e. linear, circular or elliptical) of the resultant wave is determined by the magnitudes and phase difference between the quantities E_θ^l and E_ψ^l and the direction of wave propagation. For example, if the two dipoles were fed with equal magnitude (i.e. $E_{\theta,0}^l = E_{\psi,0}^l = \frac{1}{\sqrt{2}}$) and a $\frac{\pi}{2}$ phase difference (i.e. $\zeta_\theta^l - \zeta_\psi^l = \frac{\pi}{2}$) then the polarization along the direction perpendicular to both dipole axes (the x -axis) would be circular and elliptical (or linear) in other directions (for more details see [30, Sec: 2.12]).

We can calculate the 2×2 matrix \mathbf{T}_{kl} as

$$\begin{aligned} \mathbf{T}_{kl} &= \begin{pmatrix} \hat{\theta}_{kl}^T \\ \hat{\psi}_{kl}^T \end{pmatrix} (\hat{\mathbf{z}} \hat{\mathbf{y}}) = \begin{pmatrix} \hat{\theta}_{kl}^T \hat{\mathbf{z}} & \hat{\theta}_{kl}^T \hat{\mathbf{y}} \\ \hat{\psi}_{kl}^T \hat{\mathbf{z}} & \hat{\psi}_{kl}^T \hat{\mathbf{y}} \end{pmatrix} \\ &= \frac{1}{d_{kl}} \begin{pmatrix} \sqrt{x_{kl}^2 + y_{kl}^2} & -\frac{y_{kl} z_{kl}}{\sqrt{x_{kl}^2 + y_{kl}^2}} \\ -\frac{y_{kl} z_{kl}}{\sqrt{x_{kl}^2 + z_{kl}^2}} & \sqrt{x_{kl}^2 + z_{kl}^2} \end{pmatrix}, \end{aligned} \quad (14)$$

where the matrix entries denote the polarization mismatch factors between the orientations of electric field components and the dipoles at the UAV. Using this result we obtain that

$$\begin{aligned} h_{kl}(f_0) &= \left(\mathbf{E}^l(\theta_{kl}, \psi_{kl}, f_0) \right)^H \mathbf{T}_{kl} \mathbf{E}'^k(\theta'_{kl}, \psi'_{kl}, f_0) \\ &= \frac{1}{d_{kl}} \begin{pmatrix} E_{\theta,0}^l F_\theta^l(\theta_{kl}, f_0) e^{-i\zeta_\theta^l} \\ E_{\psi,0}^l F_\psi^l(\psi_{kl}, f_0) e^{-i\zeta_\psi^l} \end{pmatrix}^T \begin{pmatrix} \sqrt{x_{kl}^2 + y_{kl}^2} & -\frac{y_{kl} z_{kl}}{\sqrt{x_{kl}^2 + y_{kl}^2}} \\ -\frac{y_{kl} z_{kl}}{\sqrt{x_{kl}^2 + z_{kl}^2}} & \sqrt{x_{kl}^2 + z_{kl}^2} \end{pmatrix} \\ &\quad \times \begin{pmatrix} E_{\theta,0}^l F_\theta'^k(\theta'_{kl}, f_0) e^{i\zeta_\theta'^k} \\ E_{\psi,0}^l F_\psi'^k(\psi'_{kl}, f_0) e^{i\zeta_\psi'^k} \end{pmatrix} \\ &= \frac{\sqrt{x_{kl}^2 + y_{kl}^2}}{d_{kl}} E_{\theta,0}^l E_{\theta,0}^l F_\theta^l(\theta_{kl}, f_0) F_\theta'^k(\theta'_{kl}, f_0) e^{i(\zeta_\theta'^k - \zeta_\theta^l)} \\ &\quad - \frac{y_{kl} z_{kl}}{d_{kl} \sqrt{x_{kl}^2 + y_{kl}^2}} E_{\theta,0}^l E_{\psi,0}^l F_\theta^l(\theta_{kl}, f_0) F_\psi'^k(\psi'_{kl}, f_0) e^{i(\zeta_\psi'^k - \zeta_\theta^l)} \\ &\quad - \frac{y_{kl} z_{kl}}{d_{kl} \sqrt{x_{kl}^2 + z_{kl}^2}} E_{\psi,0}^l E_{\theta,0}^l F_\psi^l(\psi_{kl}, f_0) F_\theta'^k(\theta'_{kl}, f_0) e^{i(\zeta_\theta'^k - \zeta_\psi^l)} \\ &\quad + \frac{\sqrt{x_{kl}^2 + z_{kl}^2}}{d_{kl}} E_{\psi,0}^l E_{\psi,0}^l F_\psi^l(\psi_{kl}, f_0) F_\psi'^k(\psi'_{kl}, f_0) e^{i(\zeta_\psi'^k - \zeta_\psi^l)}. \end{aligned} \quad (15)$$

The polarization loss factor between the transmitted electromagnetic wave and the receive antennas is given by [30]

$$\begin{aligned} \text{PLF}_{kl} &= |h_{kl}(f_0)|^2 = |\hat{\mathcal{E}}_{kl} \cdot \hat{\mathcal{E}}'_{kl}|^2 = |\hat{\mathcal{E}}_{kl}^H \hat{\mathcal{E}}'_{kl}|^2 \\ &= \hat{\mathcal{E}}_{kl}^H \hat{\mathcal{E}}'_{kl} (\hat{\mathcal{E}}_{kl})^H \hat{\mathcal{E}}'_{kl}, \end{aligned} \quad (16)$$

where $(\cdot)^H$ denotes Hermitian transpose. Note that even with fixed orientations of the transmit and receive antennas, if we move the receive antenna's position around the transmit antenna, the PLF can be high for certain elevation and azimuth angles irrespective of the type of polarization of transmit and receive antennas.

In this subsection we considered the situation when the dipoles at both transmitting and receiving end are aligned with the y - and z -axes. In the following subsection, we detail the calculation of $h_{kl}(f_0)$ due to the rotation of antennas at the transmitter and the receiver.

C. Single antenna channel transfer function for arbitrary orientation of GS and UAV antennas

Since arbitrary rotation of transmit and receive antennas change the orientation of the transmitted electric field vectors and the elevation angles, they have to be calculated with respect to the rotated coordinate axes as shown in Figure 4(a). We denote the components of rotated coordinate systems of the transmit and receive antennas using the superscripts \times and $+$, respectively. The unit direction vectors of the transmit antenna's (i.e. l -th GS antenna's) rotated coordinate system are obtained as

$$(\hat{\mathbf{x}}_l^\times \quad \hat{\mathbf{y}}_l^\times \quad \hat{\mathbf{z}}_l^\times) = (\hat{\mathbf{x}} \quad \hat{\mathbf{y}} \quad \hat{\mathbf{z}}) \mathbf{R}_l^\times (\alpha_{l,x}^\times, \alpha_{l,y}^\times, \alpha_{l,z}^\times),$$

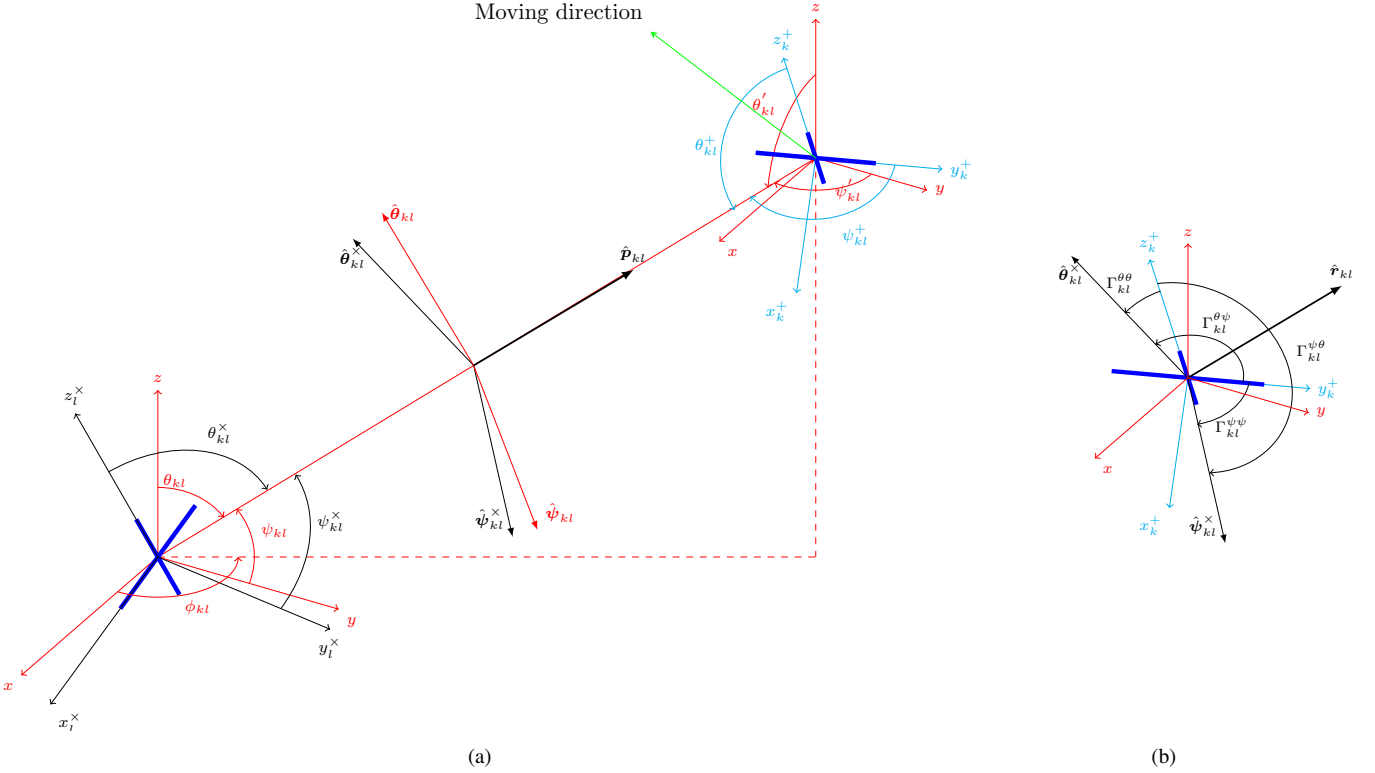


Fig. 4. (a) Schematic representation of the elevation angles measured with respect to the coordinated axes at the transmitting and receiving end. This figure also illustrates the orientation of the electric field vectors. (b) Schematic representation of the projections of the electric field vectors on UAV's dipoles.

where $\mathbf{R}_l^x(\alpha_{l,x}^x, \alpha_{l,y}^x, \alpha_{l,z}^x)$ is the 3×3 rotation matrix obtained as a function of the roll ($\alpha_{l,x}^x \in [-\frac{\pi}{2}, \frac{\pi}{2}]$), pitch ($\alpha_{l,y}^x \in [-\frac{\pi}{2}, \frac{\pi}{2}]$), and yaw ($\alpha_{l,z}^x \in [0, 2\pi]$) angles. For the calculation of this rotation matrix, see Appendix A. In this coordinate system, the receiver's (i.e. k -th UAV's) position has coordinates

$$\begin{pmatrix} x_{kl}^x \\ y_{kl}^x \\ z_{kl}^x \end{pmatrix} = \left(\mathbf{R}_l^x(\alpha_{k,x}^x, \alpha_{k,y}^x, \alpha_{k,z}^x) \right)^T \begin{pmatrix} x_{kl} \\ y_{kl} \\ z_{kl} \end{pmatrix} = \begin{pmatrix} \mathbf{R}_{l,11}^x x_{kl} + \mathbf{R}_{l,21}^x y_{kl} + \mathbf{R}_{l,31}^x z_{kl} \\ \mathbf{R}_{l,12}^x x_{kl} + \mathbf{R}_{l,22}^x y_{kl} + \mathbf{R}_{l,32}^x z_{kl} \\ \mathbf{R}_{l,13}^x x_{kl} + \mathbf{R}_{l,23}^x y_{kl} + \mathbf{R}_{l,33}^x z_{kl} \end{pmatrix}.$$

The elevation angles with respect to the rotated coordinate axes at the transmitter are calculated as $\theta_{kl}^x = \cos^{-1}(\hat{\mathbf{z}}_l^x \cdot \hat{\mathbf{p}}_{kl}) = \cos^{-1}\left(\frac{z_{kl}^x}{d_{kl}}\right)$ and $\psi_{kl}^x = \cos^{-1}(\hat{\mathbf{y}}_l^x \cdot \hat{\mathbf{p}}_{kl}) = \cos^{-1}\left(\frac{y_{kl}^x}{d_{kl}}\right)$.

Similarly, let $\mathbf{R}_k^+(\alpha_{k,x}^+, \alpha_{k,y}^+, \alpha_{k,z}^+)$ be the rotation matrix of the receive antenna. The unit direction vectors of the receive antenna's rotated coordinate system are obtained as

$$(\hat{\mathbf{x}}_k^+ \quad \hat{\mathbf{y}}_k^+ \quad \hat{\mathbf{z}}_k^+) = (\hat{\mathbf{x}} \quad \hat{\mathbf{y}} \quad \hat{\mathbf{z}}) \mathbf{R}_k^+ \left(\alpha_{k,x}^+, \alpha_{k,y}^+, \alpha_{k,z}^+ \right).$$

The elevation angles with respect to the rotated coordinate axes at the receiving end are calculated as $\theta_{kl}^+ = \cos^{-1}(\hat{\mathbf{z}}_k^+ \cdot \hat{\mathbf{p}}_{kl}') = \cos^{-1}\left(-\frac{z_{kl}^+}{d_{kl}}\right)$ and $\psi_{kl}^+ = \cos^{-1}(\hat{\mathbf{y}}_k^+ \cdot \hat{\mathbf{p}}_{kl}') = \cos^{-1}\left(-\frac{y_{kl}^+}{d_{kl}}\right)$,

where

$$\begin{pmatrix} x_{kl}^+ \\ y_{kl}^+ \\ z_{kl}^+ \end{pmatrix} = \left(\mathbf{R}_k^+ \left(\alpha_{k,x}^+, \alpha_{k,y}^+, \alpha_{k,z}^+ \right) \right)^T \begin{pmatrix} x_{kl} \\ y_{kl} \\ z_{kl} \end{pmatrix} = \begin{pmatrix} \mathbf{R}_{k,11}^+ x_{kl} + \mathbf{R}_{k,21}^+ y_{kl} + \mathbf{R}_{k,31}^+ z_{kl} \\ \mathbf{R}_{k,12}^+ x_{kl} + \mathbf{R}_{k,22}^+ y_{kl} + \mathbf{R}_{k,32}^+ z_{kl} \\ \mathbf{R}_{k,13}^+ x_{kl} + \mathbf{R}_{k,23}^+ y_{kl} + \mathbf{R}_{k,33}^+ z_{kl} \end{pmatrix}.$$

The quantity $h_{kl}(f_0)$ when we consider the rotations of the transmit and receive antennas can be calculated as in (15) to be

$$h_{kl}^{x,+}(f_0) = \left(\mathbf{E}^l(\theta_{kl}^x, \psi_{kl}^x, f_0) \right)^H \mathbf{T}_{kl}^{x,+} \mathbf{E}'^k(\theta_{kl}^+, \psi_{kl}^+, f_0), \quad (17)$$

where $\mathbf{E}^l(\theta_{kl}^x, \psi_{kl}^x, f_0)$ and $\mathbf{E}'^k(\theta_{kl}^+, \psi_{kl}^+, f_0)$ are defined similarly to (10) and (12) as

$$\mathbf{E}^l(\theta_{kl}^x, \psi_{kl}^x, f_0) = \begin{pmatrix} E_\theta^l F_\theta^l(\theta_{kl}^x, f_0) \\ E_\psi^l F_\psi^l(\psi_{kl}^x, f_0) \end{pmatrix} \quad \text{and}$$

$$\mathbf{E}'^k(\theta_{kl}^+, \psi_{kl}^+, f_0) = \begin{pmatrix} E'_\theta^k F'_\theta^k(\theta_{kl}^+, f_0) \\ E'_\psi^k F'_\psi^k(\psi_{kl}^+, f_0) \end{pmatrix},$$

and the matrix $\mathbf{T}_{kl}^{x,+}$ is

$$\mathbf{T}_{kl}^{x,+} = \begin{pmatrix} (\hat{\theta}_{kl}^x)^T \\ (\hat{\psi}_{kl}^x)^T \end{pmatrix} (\hat{\mathbf{z}}^+ \quad \hat{\mathbf{y}}^+) = \begin{pmatrix} (\hat{\theta}_{kl}^x)^T \hat{\mathbf{z}}^+ & (\hat{\theta}_{kl}^x)^T \hat{\mathbf{y}}^+ \\ (\hat{\psi}_{kl}^x)^T \hat{\mathbf{z}}^+ & (\hat{\psi}_{kl}^x)^T \hat{\mathbf{y}}^+ \end{pmatrix}.$$

Similarly to the calculation of $\hat{\theta}_{kl}$ and $\hat{\psi}_{kl}$ in (5) and (8), the unit directions of the electric fields, $\hat{\theta}_{kl}^x$ and $\hat{\psi}_{kl}^x$ can be

calculated in the rotated transmit antenna coordinate system as

$$\begin{aligned}\hat{\theta}_{kl}^x &= \frac{(\hat{x}_l^x \quad \hat{y}_l^x \quad \hat{z}_l^x)}{d_{kl}\sqrt{(x_{kl}^x)^2 + (y_{kl}^x)^2}} \begin{pmatrix} -x_{kl}^x z_{kl}^x \\ -y_{kl}^x z_{kl}^x \\ (x_{kl}^x)^2 + (y_{kl}^x)^2 \end{pmatrix} \\ &= (\hat{x} \quad \hat{y} \quad \hat{z}) \frac{\mathbf{R}_l^x (\alpha_{l,x}^x, \alpha_{l,y}^x, \alpha_{l,z}^x)}{d_{kl}\sqrt{(x_{kl}^x)^2 + (y_{kl}^x)^2}} \begin{pmatrix} -x_{kl}^x z_{kl}^x \\ -y_{kl}^x z_{kl}^x \\ (x_{kl}^x)^2 + (y_{kl}^x)^2 \end{pmatrix}\end{aligned}$$

and

$$\begin{aligned}\hat{\psi}_{kl}^x &= \frac{(\hat{x}_l^x \quad \hat{y}_l^x \quad \hat{z}_l^x)}{d_{kl}\sqrt{(x_{kl}^x)^2 + (z_{kl}^x)^2}} \begin{pmatrix} -x_{kl}^x y_{kl}^x \\ (x_{kl}^x)^2 + (z_{kl}^x)^2 \\ -y_{kl}^x z_{kl}^x \end{pmatrix} \\ &= (\hat{x} \quad \hat{y} \quad \hat{z}) \frac{\mathbf{R}_l^x (\alpha_{l,x}^x, \alpha_{l,y}^x, \alpha_{l,z}^x)}{d_{kl}\sqrt{(x_{kl}^x)^2 + (z_{kl}^x)^2}} \begin{pmatrix} -x_{kl}^x y_{kl}^x \\ (x_{kl}^x)^2 + (z_{kl}^x)^2 \\ -y_{kl}^x z_{kl}^x \end{pmatrix}.\end{aligned}$$

Obviously, for the receive antenna dipole directions we have

$$\begin{aligned}\hat{z}_k^+ &= (\hat{x}_k^+ \quad \hat{y}_k^+ \quad \hat{z}_k^+) (0 \quad 0 \quad 1)^T \\ &= (\hat{x} \quad \hat{y} \quad \hat{z}) \mathbf{R}_k^+ (\alpha_{k,x}^+, \alpha_{k,y}^+, \alpha_{k,z}^+) (0 \quad 0 \quad 1)^T\end{aligned}$$

and

$$\begin{aligned}\hat{y}_k^+ &= (\hat{x}_k^+ \quad \hat{y}_k^+ \quad \hat{z}_k^+) (0 \quad 1 \quad 0)^T \\ &= (\hat{x} \quad \hat{y} \quad \hat{z}) \mathbf{R}_k^+ (\alpha_{k,x}^+, \alpha_{k,y}^+, \alpha_{k,z}^+) (0 \quad 1 \quad 0)^T\end{aligned}$$

Since the reference coordinate system is orthonormal, i.e. $(\hat{x} \quad \hat{y} \quad \hat{z})^T (\hat{x} \quad \hat{y} \quad \hat{z}) = \mathbf{I}_3$, we calculate the matrix $\mathbf{T}_{kl}^{x,+}$ as

$$\begin{aligned}\mathbf{T}_{kl}^{x,+} &= \begin{pmatrix} (\hat{\theta}_{kl}^x)^T \\ (\hat{\psi}_{kl}^x)^T \end{pmatrix} (\hat{z}^+ \quad \hat{y}^+) \\ &= \frac{1}{d_{kl}} \begin{pmatrix} -\frac{x_{kl}^x z_{kl}^x}{\sqrt{(x_{kl}^x)^2 + (y_{kl}^x)^2}} & -\frac{y_{kl}^x z_{kl}^x}{\sqrt{(x_{kl}^x)^2 + (y_{kl}^x)^2}} & \sqrt{(x_{kl}^x)^2 + (y_{kl}^x)^2} \\ -\frac{x_{kl}^x y_{kl}^x}{\sqrt{(x_{kl}^x)^2 + (z_{kl}^x)^2}} & \sqrt{(x_{kl}^x)^2 + (z_{kl}^x)^2} & -\frac{z_{kl}^x y_{kl}^x}{\sqrt{(x_{kl}^x)^2 + (z_{kl}^x)^2}} \end{pmatrix} \\ &\quad \times \mathbf{R}_{kl}^{x,+} \begin{pmatrix} 0 & 0 \\ 0 & 1 \\ 1 & 0 \end{pmatrix},\end{aligned}\tag{18}$$

where $\mathbf{R}_{kl}^{x,+}$ is the combined rotation matrix given by

$$\begin{aligned}\mathbf{R}_{kl}^{x,+} &= \left(\mathbf{R}_l^x (\alpha_{l,x}^x, \alpha_{l,y}^x, \alpha_{l,z}^x) \right)^T \mathbf{R}_k^+ (\alpha_{k,x}^+, \alpha_{k,y}^+, \alpha_{k,z}^+) \\ &= \begin{pmatrix} \mathbf{R}_{kl,11}^{x,+} & \mathbf{R}_{kl,12}^{x,+} & \mathbf{R}_{kl,13}^{x,+} \\ \mathbf{R}_{kl,21}^{x,+} & \mathbf{R}_{kl,22}^{x,+} & \mathbf{R}_{kl,23}^{x,+} \\ \mathbf{R}_{kl,31}^{x,+} & \mathbf{R}_{kl,32}^{x,+} & \mathbf{R}_{kl,33}^{x,+} \end{pmatrix}.\end{aligned}$$

Note that the elements of $\mathbf{T}_{kl}^{x,+}$ are the projections of the unit electric field vectors components $\hat{\theta}_{kl}^x$ and $\hat{\psi}_{kl}^x$ on the receive dipoles unit vectors \hat{z}_k^+ and \hat{y}_k^+ as shown in Figure 4(b), i.e.

$$\mathbf{T}_{kl}^{x,+} = \begin{pmatrix} \cos \Gamma_{kl}^{\theta\theta} & \cos \Gamma_{kl}^{\theta\psi} \\ \cos \Gamma_{kl}^{\psi\theta} & \cos \Gamma_{kl}^{\psi\psi} \end{pmatrix}.\tag{19}$$

The magnitudes of these projections are

$$\begin{aligned}\cos \Gamma_{kl}^{\theta\theta} &= \hat{\theta}_{kl}^x \cdot \hat{z}_k^+ \\ &= \frac{-\mathbf{R}_{kl,13}^{x,+} x_{kl}^x z_{kl}^x - \mathbf{R}_{kl,23}^{x,+} y_{kl}^x z_{kl}^x + \mathbf{R}_{kl,33}^{x,+} ((x_{kl}^x)^2 + (y_{kl}^x)^2)}{d_{kl} \sqrt{(x_{kl}^x)^2 + (y_{kl}^x)^2}}, \\ \cos \Gamma_{kl}^{\theta\psi} &= \hat{\theta}_{kl}^x \cdot \hat{y}_k^+ \\ &= \frac{-\mathbf{R}_{kl,12}^{x,+} x_{kl}^x z_{kl}^x - \mathbf{R}_{kl,22}^{x,+} y_{kl}^x z_{kl}^x + \mathbf{R}_{kl,32}^{x,+} ((x_{kl}^x)^2 + (y_{kl}^x)^2)}{d_{kl} \sqrt{(x_{kl}^x)^2 + (y_{kl}^x)^2}}, \\ \cos \Gamma_{kl}^{\psi\theta} &= \hat{\psi}_{kl}^x \cdot \hat{z}_k^+ \\ &= \frac{-\mathbf{R}_{kl,13}^{x,+} x_{kl}^x y_{kl}^x - \mathbf{R}_{kl,33}^{x,+} z_{kl}^x y_{kl}^x + \mathbf{R}_{kl,23}^{x,+} ((x_{kl}^x)^2 + (z_{kl}^x)^2)}{d_{kl} \sqrt{(x_{kl}^x)^2 + (z_{kl}^x)^2}}, \\ \cos \Gamma_{kl}^{\psi\psi} &= \hat{\psi}_{kl}^x \cdot \hat{y}_k^+ \\ &= \frac{-\mathbf{R}_{kl,12}^{x,+} x_{kl}^x y_{kl}^x - \mathbf{R}_{kl,32}^{x,+} z_{kl}^x y_{kl}^x + \mathbf{R}_{kl,22}^{x,+} ((x_{kl}^x)^2 + (z_{kl}^x)^2)}{d_{kl} \sqrt{(x_{kl}^x)^2 + (z_{kl}^x)^2}}.\end{aligned}$$

It can be verified that if the transmit and receive antennas are not rotated, i.e. when $\mathbf{R}_{kl}^{x,+} = \mathbf{I}_3$, the 2×2 matrix in (18) is equal to (14).

D. Antenna array channel model

From (4), the $M \times 1$ channel vector from the k -th UAV at position P_k to the GS array with carrier frequency $f_0 = f_c$ is given by

$$\mathbf{g}_k = [g_{k1} \ g_{k2} \ \dots \ g_{kM}]^T,\tag{20}$$

where the elements are obtained from (4) as

$$g_{kl} = \sqrt{\beta_{kl}} h_{kl} e^{-i \frac{2\pi}{\lambda} d_{kl}}, \quad l = 1, 2, \dots, M,$$

where the complex quantity h_{kl} incorporates the transmit and receive dipoles' antenna gain and field patterns, and the polarization mismatch loss factors, i.e. $h_{kl} = \sqrt{\mathcal{G}_t \mathcal{G}_r} h_{kl}^{x,+}(f_c)$, where \mathcal{G}_t and \mathcal{G}_r are the gains of transmit and receive dipole, respectively, and $h_{kl}^{x,+}(f_c)$ is given in (17). Note that we introduced \mathcal{G}_t and \mathcal{G}_r here, because the field patterns are normalized in (7). For half-wavelength dipole, the antenna gain is approximately equal to 1.643 (≈ 2.15 dB). Irrespective of the type of UAV, depending on the placement of the antenna, the UAV's body may also introduce additional loss. For example, measurement results show that the body blockage loss in fixed-wing aircraft is between 5 to 35 dB [31] and in quadcopters it is between 5 to 15 dB [5]. For simplicity of the analysis, in our model, we do not include the body blockage loss. However, it could be incorporated in the model as a function of the azimuth, elevation, roll, pitch, and yaw angles.

E. Uplink pilot signaling and channel estimation

For the purpose of receiver processing, the GS need to know the CSI. Since the UAVs move in a 3D space with high speed, the signal received at the GS will experience Doppler shift. Therefore, the channel vectors at the GS have to be re-estimated after certain time duration, i.e. coherence time. The

coherence time is defined as a time interval over which the impact of Doppler shift on the received signal is insignificant. We adopt an over-conservative design to re-estimate the channel after every coherence time T_{coh} calculated as follows. Given the maximum speed of the UAVs v_{\max} , the coherence time can be calculated as $T_{\text{coh}} \approx \frac{1}{2f_{\max}}$, where the Doppler frequency $f_{\max} = \frac{v_{\max}}{\lambda}$. For example, if the maximum speed of UAV is 30 m/s, at a carrier frequency of 2.4 GHz, the coherence time is $T_{\text{coh}} \approx 2$ ms.

As the massive MIMO systems operate in TDD mode, downlink transmission, uplink pilot transmission, and uplink data transmission happen within the coherence interval T_{len} , i.e. $\tau_{\text{dl}} + \tau_{\text{ul,p}} + \tau_{\text{ul,d}} \leq T_{\text{len}}$. The parameters τ_{dl} , $\tau_{\text{ul,p}}$, and $\tau_{\text{ul,d}}$ denote the number of symbols used for downlink, uplink pilot, and uplink data transmission, respectively. The coherence interval T_{len} is defined as the product of coherence time and coherence bandwidth. In LoS, since there is no multipath, the coherence bandwidth is infinite. However, in over-water and mountainous settings, due to a few multipath components, the coherence bandwidth is finite [32]–[34]⁴. Therefore, we define

$$T_{\text{len}} = T_{\text{coh}} \times B_c = \frac{B_c \cdot c}{2 \cdot v_{\max} \cdot f_c}, \quad (21)$$

where B_c is the coherence bandwidth.

During the training phase, K UAVs are assigned K orthogonal pilot sequences of length $\tau_{\text{ul,p}}$. Let the $M \times K$ channel matrix between the GS and the UAVs be $\mathbf{G} = [\mathbf{g}_1 \mathbf{g}_2 \dots \mathbf{g}_K]$. The $M \times \tau_{\text{ul,p}}$ received pilot matrix at the GS is given by

$$\mathbf{Y}_p = \sqrt{p_p} \mathbf{G} \Phi^T + \mathbf{N}_p,$$

where p_p is transmit power of each pilot symbol, Φ is $\tau_{\text{ul,p}} \times K$ orthogonal pilot matrix satisfies $\Phi^H \Phi = \mathbf{I}_K$ and \mathbf{N}_p is $M \times \tau_{\text{ul,p}}$ noise matrix with i.i.d $\mathcal{CN}(0, 1)$ elements. For notational convenience, we take noise variance to be 1. Therefore, p_p can be interpreted as normalized transmit SNR.

In order to obtain reliable channel estimate, the pilot power has to be chosen based on the worst-case values of the distance and effective antenna gain,

$$p_p = \rho_p \left(\frac{4\pi d_{\text{wc}}}{\lambda} \right)^2 \frac{1}{\chi_{\text{wc}}}, \quad (22)$$

where ρ_p is the target pilot SNR, d_{wc} is the maximum possible distance between the GS and UAV, and χ_{wc} is the lowest possible gain over all possible values of azimuth, elevation, and UAV's rotation angles as discussed in Appendix A, i.e. $\chi_{\text{wc}} = \min_{\phi, \theta, \alpha_x, \alpha_y, \alpha_z} \frac{1}{M} \sum_{l=1}^M \chi_{kl}$.

⁴Recent measurements performed in the C-band (5.03–5.091 GHz) show that the average root-mean-square delay spread is typically very small in over-water (~ 10 ns), hilly and mountain (~ 10 ns), suburban and near-urban (10–60 ns) environments (with an average UAV altitude of 600 m and link ranges from 860 m to several kilometers) [32]–[34]. Hence, if the coherence bandwidth is defined as the bandwidth over which the frequency correlation function is above 0.5 [35], depending on the environment the coherence bandwidth varies between 3 MHz and 20 MHz (300 KHz and 2 MHz if the frequency correlation is 0.9). Further, the measured values of Rician K -factors in different environments is greater than 25 dB [32]–[34]. Therefore, it is appropriate to consider LoS propagation between the GS and the UAVs.

The maximum likelihood (ML) estimate of \mathbf{G} given \mathbf{Y}_p is

$$\hat{\mathbf{G}} = \frac{1}{\sqrt{p_p}} \mathbf{Y}_p \Phi^* = \mathbf{G} + \frac{1}{\sqrt{p_p}} \mathbf{W}. \quad (23)$$

Here, $\mathbf{W} = \mathbf{N}_p \Phi^*$ is the estimation error that is uncorrelated with \mathbf{G} . The elements of \mathbf{W} are i.i.d zero-mean complex Gaussian with unit variance. We use ML as finding the minimum mean square error estimate is nontrivial under the assumed LoS model.

F. Uplink Data Transmission

The $M \times 1$ received signal vector at the GS is given by

$$\mathbf{y} = \mathbf{G}(\sqrt{p_u} \odot \mathbf{q}) + \mathbf{n},$$

where \odot denotes element wise multiplication; \mathbf{q} is the vector of symbols simultaneously transmitted by the K UAVs, i.e. $\mathbf{q} = [q_1, q_2, \dots, q_K]^T$ (normalized such that $\mathbb{E}\{|q_k|^2\} = 1$ for all $k \in \{1, 2, \dots, K\}$); $\mathbf{p}_u = [p_{u1}, p_{u2}, \dots, p_{uK}]^T$ is the vector of transmit power of symbols of K UAVs; \mathbf{n} is a complex AWGN vector, $\mathbf{n} \sim \mathcal{CN}(0, \mathbf{I}_M)$.

In order to maintain the same average SNR (ρ_u) for all UAVs, we consider channel inversion power control, i.e. the power allocated by the k -th UAV to each data symbol is

$$p_{uk} = \min \left(\frac{\rho_u}{\frac{1}{M} \sum_{l=1}^M \beta_{kl} \chi_{kl}}, p_u \right), \quad (24)$$

where $\chi_{kl} = |h_{kl}|^2$ and p_u is the maximum power available at the UAV for data symbol. Note that for power control, the UAV needs to know the large scale channel gain (i.e. the denominator term in (24)). This can be accomplished through downlink pilot transmission. Unlike uplink, the downlink pilot transmission requires only one symbol.

We consider that the pilot symbols are transmitted with fixed power p_p according to (22). The value of data power p_u is calculated from the total energy constraint \mathcal{P} of each UAV in a coherence interval given by

$$p_p \tau_{\text{ul,p}} + p_u \tau_{\text{ul,d}} \leq \mathcal{P}. \quad (25)$$

Here \mathcal{P} is a design parameter selected based on source of power supply and flying range of the UAVs. Due to the uplink power constraint in (24), the combined effect of free-space path loss, polarization mismatch, and directional antenna gains may result in signal outage, i.e. the k -th UAV is in outage if $\frac{\rho_u}{\frac{1}{M} \sum_{l=1}^M \beta_{kl} \chi_{kl}} > p_u$. The outage probability is defined as

$$P_{\text{out}} = \mathbb{P} \left(\frac{\rho_u}{\frac{1}{M} \sum_{l=1}^M \beta_{kl} \chi_{kl}} > p_u \right). \quad (26)$$

When the GS array elements are identically oriented and the distance between the GS and the UAV location (i.e. d_k) is much larger than the aperture size of the GS array, h_{kl} and β_{kl} are approximately the same across the antenna elements, i.e. for all $l = 1, 2, \dots, M$, we have

$$h_{kl} \approx h_k, \beta_{kl} \approx \beta_k, \mathbf{R}_{kl}^{\times,+} = \mathbf{I}_3, \text{ and} \\ d_{kl} \gg \sqrt{(M_x - 1)^2 \delta_x^2 + (M_y - 1)^2 \delta_y^2}. \quad (27)$$

Therefore, from (24), we obtain that

$$p_{uk} = \min \left(\frac{\rho_u}{\beta_k \chi_k}, p_u \right). \quad (28)$$

For analytical tractability, we use (27) and (28) for the ergodic rate analysis in Section III. In Section V, we separately show the impact of arbitrary orientation of GS array elements on the link reliability.

III. ACHIEVABLE RATE ANALYSIS

It is known that the linear detectors (MRC and ZF) perform fairly well when $K \ll M$ [13]. In this section, we derive the uplink achievable rate for MRC receiver considering the estimated CSI. For ZF receiver, we analyze the achievable rate considering perfect CSI.

A. MRC receiver

By using the MRC detector, the received signal \mathbf{y} is separated into K streams by multiplying it with $\hat{\mathbf{G}}^H$ as follows

$$\mathbf{r} = \hat{\mathbf{G}}^H \mathbf{y} = \hat{\mathbf{G}}^H \mathbf{G} (\sqrt{p_u} \odot \mathbf{q}) + \hat{\mathbf{G}}^H \mathbf{n}.$$

Let r_k and q_k be the k -th elements of the vectors \mathbf{r} and \mathbf{q} , respectively. Then,

$$r_k = \sqrt{p_{uk}} \hat{\mathbf{g}}_k^H \mathbf{g}_k q_k + \sum_{j=1, j \neq k}^K \sqrt{p_{uj}} \hat{\mathbf{g}}_k^H \mathbf{g}_j q_j + \hat{\mathbf{g}}_k^H \mathbf{n}, \quad (29)$$

where $\hat{\mathbf{g}}_k$ is the k -th column of $\hat{\mathbf{G}}$. In (29), the quantities \mathbf{g}_k and \mathbf{g}_j will be continuously changing as the positions of the UAVs change due to their movement. Even if the location of the k -th UAV is fixed, it is more likely that any of the other $K - 1$ UAVs will interfere that UAV. Hence, the quantity $\hat{\mathbf{g}}_k^H \mathbf{g}_j$ will also be changing as a function of the positions of the UAVs i.e. d_k , θ_k , and ϕ_k for all $k \in \{1, 2, \dots, K\}$. For example, in micro UAV networks [5], since the UAVs move at high speed (10 m/s to 30 m/s) in random directions, one can expect multiple independent realizations of $\mathbf{g}_k^H \mathbf{g}_j$ within a short time duration. For example, consider an ULA with M_x antennas on the x -axis and $M_y = 1$, i.e. $M = M_x$. If d_k and d_j are very large when compared to the aperture size of the array, after some manipulations, the square of the inner product between the channel vectors of the k -th and the j -th UAV can be obtained from (20) and (27) as

$$|\mathbf{g}_k^H \mathbf{g}_j|^2 = \beta_k \beta_j \chi_k \chi_j M^2 \times \frac{\text{sinc}^2(M \frac{\delta_x}{\lambda} (\sin \theta_k \cos \phi_k - \sin \theta_j \cos \phi_j))}{\text{sinc}^2(\frac{\delta_x}{\lambda} (\sin \theta_k \cos \phi_k - \sin \theta_j \cos \phi_j))}.$$

Here $\text{sinc}(x) = \frac{\sin(\pi x)}{\pi x}$. The fluctuations in $|\mathbf{g}_k^H \mathbf{g}_j|^2$ are determined by the following factors: number of antennas, M , antenna spacing, δ_x , velocity, and moving direction of the UAVs. Therefore, by assuming multiple independent realizations of the interference power within the codeword transmission time, we compute the ergodic rate by averaging over all possible UAV positions.

Next we derive closed form expression for achievable rate using the method from [13] i.e. we assume that the receiver at the GS uses only statistical knowledge of the channel when

performing the detection. The k -th element of \mathbf{r} in (29), i.e. r_k , can be rewritten in the form

$$\begin{aligned} \sqrt{p_{uk}} r_k &= \mathbb{E}\{p_{uk} \hat{\mathbf{g}}_k^H \mathbf{g}_k\} q_k + (p_{uk} \hat{\mathbf{g}}_k^H \mathbf{g}_k - \mathbb{E}\{p_{uk} \hat{\mathbf{g}}_k^H \mathbf{g}_k\}) q_k \\ &\quad + \sum_{j=1, j \neq k}^K \sqrt{p_{uj} p_{uk}} \hat{\mathbf{g}}_k^H \mathbf{g}_j q_j + \sqrt{p_{uk}} \hat{\mathbf{g}}_k^H \mathbf{n}. \end{aligned} \quad (30)$$

By defining the effective additive noise as

$$\begin{aligned} a'_k &= \underbrace{\left(p_{uk} \hat{\mathbf{g}}_k^H \mathbf{g}_k - \mathbb{E}\{p_{uk} \hat{\mathbf{g}}_k^H \mathbf{g}_k\} \right) q_k}_{a_1} \\ &\quad + \underbrace{\sum_{j=1, j \neq k}^K \sqrt{p_{uj} p_{uk}} \hat{\mathbf{g}}_k^H \mathbf{g}_j q_j}_{a_2} + \underbrace{\sqrt{p_{uk}} \hat{\mathbf{g}}_k^H \mathbf{n}}_{a_3}, \end{aligned} \quad (31)$$

the expression in (30) can be written as

$$\sqrt{p_{uk}} r_k = \mathbb{E}\{p_{uk} \hat{\mathbf{g}}_k^H \mathbf{g}_k\} q_k + a'_k. \quad (32)$$

Since $\mathbb{E}\{\hat{\mathbf{g}}_k^H \mathbf{g}_k\}$ is deterministic and q_k is independent of $\hat{\mathbf{g}}_k^H \mathbf{g}_k$, the first two terms of (30) are uncorrelated. Similarly, the last two terms of (30) are uncorrelated with the first term of (30). Hence, the desired signal and the effective additive noise in (32) are uncorrelated. By using the fact that the worst-case uncorrelated additive noise is independent Gaussian noise of same variance [13], the ergodic rate achieved by the k -th UAV can be lower bounded as

$$S_k^{\text{MRC}} \geq S_k^{\text{lb,MRC}} \triangleq \Lambda \log_2 \left(1 + \frac{|\mathbb{E}\{p_{uk} \hat{\mathbf{g}}_k^H \mathbf{g}_k\}|^2}{\text{var}(a'_k)} \right), \quad (33)$$

where Λ denotes the fraction of symbols used for uplink data transmission within the coherence length and $p_{uk} \leq p_u$. If the number of uplink pilot symbols $\tau_{\text{ul,p}} = K$, then from (21) we can write

$$\Lambda = 1 - \frac{\tau_{\text{dl}} + \tau_{\text{ul,p}}}{T_{\text{len}}} = 1 - \frac{2 \cdot v_{\max} \cdot f_c \cdot (\tau_{\text{dl}} + K)}{B_c \cdot c}. \quad (34)$$

Since all three terms in (31) are independent of each other, the variance of effective noise in (33) is $\text{var}(a'_k) = \text{var}(a_1) + \text{var}(a_2) + \text{var}(a_3)$. After substituting the expectation and variance terms in (33), the lower bound $S_k^{\text{lb,MRC}}$ of the ergodic rate achieved by the k -th UAV is obtained as given in (35) (shown on top of next page). For the proof, see Appendix B.

In (35), it can be observed that the numerator term inside the logarithm increases proportionally with M . This is an effect of the array gain. For example, with 100 antennas and the same radiated power as in a single-antenna system, the array gain is 20 dB which implies a range extension of 10 times in LoS. The first term in the denominator represents the cumulative interference caused by the other $K - 1$ UAVs. The second and third terms stem from channel estimation errors and noise, respectively.

Equation (35) can be used to analyze the achievable rate for any arbitrary distribution and placement of the drones (i.e. distributions of d_k , θ_k , and ϕ_k for $k \in \{1, 2, \dots, K\}$). For some distributions one may have to compute the ergodic rate numerically as it is difficult to obtain a closed form expression. Next we derive a lower bound on the ergodic rate for the case

$$S_k^{\text{lb},\text{MRC}} = \Lambda \log_2 \left(1 + \frac{M\rho_u}{\frac{1}{M\rho_u} \sum_{j=1,j \neq k}^K \mathbb{E}\{p_{uj}p_{uk}|\mathbf{g}_k^H \mathbf{g}_j|^2\} + (1+K\rho_u)\mathbb{E}\left\{\frac{1}{\beta_k \chi_k}\right\} \left(\frac{\lambda}{4\pi d_{\text{wc}}}\right)^2 \frac{\chi_{\text{wc}}}{\rho_u \rho_p} + 1} \right). \quad (35)$$

with uniformly distributed UAV locations inside a spherical shell and the results follow in closed form in this case.

Theorem 3.1: By employing MRC receiver at the GS and using the ML estimate of the channel matrix, for the independently and spherically uniformly distributed UAV locations inside the spherical shell with inner radius

$$R_{\min} > \sqrt{(M_x - 1)^2 \delta_x^2 + (M_y - 1)^2 \delta_y^2} \quad (36)$$

and outer radius R , the lower bound on the achievable ergodic rate for the k -th UAV is given in (37) (shown on top of next page).

Proof: Consider that the UAV positions are independently and spherically uniformly distributed within a spherical shell with inner radius radius R_{\min} and outer radius R . The distribution of the distance d_j (for all $j \in \{1, 2, \dots, K\}$) is given by

$$f_{d_j}(r) = \frac{3r^2}{R^3 - R_{\min}^3}, \quad R_{\min} \leq r \leq R. \quad (42)$$

The distributions of the elevation and azimuth angles are given by

$$f_{\theta_j}(\theta) = \frac{\sin \theta}{2}, \quad 0 \leq \theta \leq \pi \quad \text{and} \quad f_{\phi_j}(\phi) = \frac{1}{2\pi}, \quad 0 \leq \phi \leq 2\pi, \quad (43)$$

respectively.

By using (42), since χ_k is independent of the distance (in spherical coordinates χ_k is only a function of θ_k and ϕ_k), the expected value of $\frac{1}{\beta_k \chi_k}$ can be obtained as

$$\begin{aligned} \mathbb{E}\left\{\frac{1}{\beta_k \chi_k}\right\} &= \mathbb{E}\left\{\left(\frac{4\pi d_k}{\lambda}\right)^2\right\} \mathbb{E}\left\{\frac{1}{\chi_k}\right\} \\ &= \mathbb{E}\left\{\frac{1}{\chi_k}\right\} \left(\frac{4\pi}{\lambda}\right)^2 \int_{R_{\min}}^R r^2 f_{d_k}(r) dr \\ &= \mathbb{E}\left\{\frac{1}{\chi_k}\right\} \left(\frac{4\pi}{\lambda}\right)^2 \int_{R_{\min}}^R r^2 \frac{3r^2}{R^3 - R_{\min}^3} dr \\ &= \left(\frac{4\pi}{\lambda}\right)^2 \kappa \frac{3(R^5 - R_{\min}^5)}{5(R^3 - R_{\min}^3)}, \end{aligned} \quad (44)$$

where $\kappa = \mathbb{E}\left\{\frac{1}{\chi_k}\right\}$. This expectation has to be calculated numerically as h_{kl} is a complicated function of rotation angles, field patterns, and polarization mismatch factors. We will discuss this in detail in Section V.

The inner product between the channel vectors of k -th and j -th UAVs can be written as

$$\mathbf{g}_k^H \mathbf{g}_j = \sum_{l=1}^M \sqrt{\beta_{kl} \beta_{jl}} h_{kl} h_{jl} e^{i \frac{2\pi}{\lambda} (d_{kl} - d_{jl})}. \quad (45)$$

By applying (27), the expression in (45) can be rewritten as

$$\mathbf{g}_k^H \mathbf{g}_j = \sqrt{\beta_k \beta_j} h_k h_j \sum_{l=1}^M e^{i \frac{2\pi}{\lambda} (d_{kl} - d_{jl})}.$$

Since $|\mathbf{g}_k^H \mathbf{g}_j|^2 = (\mathbf{g}_k^H \mathbf{g}_j)(\mathbf{g}_k^H \mathbf{g}_j)^H$, we can write

$$\begin{aligned} |\mathbf{g}_k^H \mathbf{g}_j|^2 &= \beta_k \beta_j |h_k|^2 |h_j|^2 \\ &\times \left(\sum_{l=1}^M e^{i \frac{2\pi}{\lambda} (d_{kl} - d_{jl})} \right) \left(\sum_{l'=1}^M e^{-i \frac{2\pi}{\lambda} (d_{kl'} - d_{jl'})} \right) \\ &= \beta_k \beta_j \chi_k \chi_j \sum_{l=1}^M \sum_{l'=1}^M e^{i \frac{2\pi}{\lambda} (d_{kl} - d_{kl'})} e^{-i \frac{2\pi}{\lambda} (d_{jl} - d_{jl'})}. \end{aligned}$$

The expectation of $p_{uj}p_{uk}|\mathbf{g}_k^H \mathbf{g}_j|^2$ can be written as

$$\begin{aligned} \mathbb{E}\{p_{uj}p_{uk}|\mathbf{g}_k^H \mathbf{g}_j|^2\} &= \mathbb{E}\left\{(p_{uk} \beta_k \chi_k)(p_{uj} \beta_j \chi_j)\right. \\ &\quad \left. \times \sum_{l=1}^M \sum_{l'=1}^M e^{i \frac{2\pi}{\lambda} (d_{kl} - d_{kl'})} e^{-i \frac{2\pi}{\lambda} (d_{jl} - d_{jl'})}\right\}. \end{aligned} \quad (46)$$

Since d_{kl} and d_{jl} are independent, by applying (28), the expectation in (46) can be written as

$$\mathbb{E}\{p_{uj}p_{uk}|\mathbf{g}_k^H \mathbf{g}_j|^2\} = \rho_u^2 \sum_{l=1}^M \sum_{l'=1}^M N_{kl} N_{jl}^*,$$

where

$$N_{kl} = \mathbb{E}\{e^{i \frac{2\pi}{\lambda} (d_{kl} - d_{kl'})}\} \quad \text{and} \quad N_{jl} = \mathbb{E}\{e^{-i \frac{2\pi}{\lambda} (d_{jl} - d_{jl'})}\}.$$

Obviously $N_{kl} = N_{jl}$. Therefore,

$$\begin{aligned} \mathbb{E}\{p_{uj}p_{uk}|\mathbf{g}_k^H \mathbf{g}_j|^2\} &= \rho_u^2 \sum_{l=1}^M \sum_{l'=1}^M |N_{kl}|^2 \\ &= \rho_u^2 \left(M + \sum_{l=1}^M \sum_{l'=1, l' \neq l}^M |N_{kl}|^2 \right). \end{aligned} \quad (47)$$

The distance difference between the l -th and l' -th elements to the k -th UAV is given by

$$\begin{aligned} d_{kl} - d_{kl'} &= \frac{1}{2d_k} \left[((p-1)^2 - (p'-1)^2) \delta_x^2 + ((q-1)^2 - (q'-1)^2) \delta_y^2 \right] \\ &\quad - \sin \theta_k \left[(p-p') \delta_x \cos \phi_k + (q-q') \delta_y \sin \phi_k \right]. \end{aligned}$$

Since d_k , θ_k , and ϕ_k are independent for all $k \in \{1, 2, \dots, K\}$,

$$\begin{aligned} N_{kl} &= \mathbb{E}\left\{e^{i \frac{2\pi}{\lambda} (d_{kl} - d_{kl'})}\right\} \\ &= \mathbb{E}\left\{e^{i \frac{\pi}{\lambda} \frac{1}{d_k} [((p-1)^2 - (p'-1)^2) \delta_x^2 + ((q-1)^2 - (q'-1)^2) \delta_y^2]}\right\} \\ &\quad \times \mathbb{E}\left\{e^{-i \frac{2\pi}{\lambda} \sin \theta_k [(p-p') \delta_x \cos \phi_k + (q-q') \delta_y \sin \phi_k]}\right\}. \end{aligned} \quad (48)$$

$$S_k^{\text{lb},\text{MRC}} = \Lambda \log_2 \left(1 + \frac{M\rho_u}{\rho_u(K-1)(1+\frac{\Omega}{M}) + 1 + \frac{1}{\rho_u\rho_p}(1+K\rho_u)^{\frac{3\kappa\chi_{\text{wc}}(R^5-R_{\min}^5)}{5R^2(R^3-R_{\min}^3)}}} \right), \quad (37)$$

where

$$\Omega = \sum_{l=1}^M \sum_{l'=1, l' \neq l}^M \left\{ \text{sinc}^2 \left(\frac{2}{\lambda} \sqrt{(p'-p)^2\delta_x^2 + (q'-q)^2\delta_y^2} \right) \times (\mathbb{C}^2(b_{ll'}) + \mathbb{D}^2(b_{ll'})) \right\}, \quad (38)$$

$$b_{ll'} = \frac{\pi}{\lambda} ((p-1)^2 - (p'-1)^2)\delta_x^2 + ((q-1)^2 - (q'-1)^2)\delta_y^2, \quad (39)$$

$$l = (q-1)M_x + p, \quad l' = (q'-1)M_x + p', \quad p, p' \in \{1, 2, \dots, M_x\}, \quad q, q' \in \{1, 2, \dots, M_y\},$$

$$\begin{aligned} \mathbb{C}(b_{ll'}) &= \frac{1}{2(R^3 - R_{\min}^3)} \times \left((2R^2 - b_{ll'}^2)R \cos(b_{ll'}/R) - b_{ll'}R^2 \sin(b_{ll'}/R) - b_{ll'}^3 \text{Si}(b_{ll'}/R) \right. \\ &\quad \left. - (2R_{\min}^2 - b_{ll'}^2)R_{\min} \cos(b_{ll'}/R_{\min}) + b_{ll'}R_{\min}^2 \sin(b_{ll'}/R_{\min}) + b_{ll'}^3 \text{Si}(b_{ll'}/R_{\min}) \right), \end{aligned} \quad (40)$$

$$\begin{aligned} \mathbb{D}(b_{ll'}) &= \frac{1}{2(R^3 - R_{\min}^3)} \times \left((2R^2 - b_{ll'}^2)R \sin(b_{ll'}/R) + b_{ll'}R^2 \cos(b_{ll'}/R) + b_{ll'}^3 \text{Ci}(b_{ll'}/R) \right. \\ &\quad \left. - (2R_{\min}^2 - b_{ll'}^2)R_{\min} \sin(b_{ll'}/R_{\min}) - b_{ll'}R_{\min}^2 \cos(b_{ll'}/R_{\min}) - b_{ll'}^3 \text{Ci}(b_{ll'}/R_{\min}) \right), \end{aligned} \quad (41)$$

and $\kappa = \mathbb{E} \left\{ \frac{1}{\chi_k} \right\}$. Here, $\text{Si}(x) = \int_0^x \frac{\sin t}{t} dt$ and $\text{Ci}(x) = -\int_x^\infty \frac{\cos t}{t} dt$.

By using (42), the first expectation in (48) can be obtained as

$$\begin{aligned} \mathbb{E} \left\{ e^{i\frac{\pi}{\lambda} \frac{1}{d_k} [((p-1)^2 - (p'-1)^2)\delta_x^2 + ((q-1)^2 - (q'-1)^2)\delta_y^2]} \right\} \\ = \mathbb{C}(b_{ll'}) + i \mathbb{D}(b_{ll'}), \end{aligned} \quad (49)$$

where $b_{ll'}$, $\mathbb{C}(b_{ll'})$, and $\mathbb{D}(b_{ll'})$ are defined in (39), (40), (41), respectively.

By using (43), the second expectation in (48) can be obtained as

$$\begin{aligned} \mathbb{E} \left\{ e^{-i\frac{2\pi}{\lambda} \sin \theta_k [(p-p')\delta_x \cos \phi_k + (q-q')\delta_y \sin \phi_k]} \right\} \\ = \text{sinc} \left(\frac{2}{\lambda} \sqrt{(p'-p)^2\delta_x^2 + (q'-q)^2\delta_y^2} \right). \end{aligned} \quad (50)$$

For the proofs of (49) and (50), see Appendix C.

By substituting (49) and (50) into (48), we obtain that

$$\begin{aligned} N_{kll'} &= (\mathbb{C}(b_{ll'}) + i \mathbb{D}(b_{ll'})) \\ &\quad \times \text{sinc} \left(\frac{2}{\lambda} \sqrt{(p'-p)^2\delta_x^2 + (q'-q)^2\delta_y^2} \right). \end{aligned} \quad (51)$$

By substituting (51) into (47), we get

$$\mathbb{E} \left\{ p_{uj} p_{uk} |\mathbf{g}_k^H \mathbf{g}_j|^2 \right\} = \rho_u^2 (M + \Omega), \quad (52)$$

where

$$\begin{aligned} \Omega &= \sum_{l=1}^M \sum_{l'=1, l' \neq l}^M \left\{ \text{sinc}^2 \left(\frac{2}{\lambda} \sqrt{(p'-p)^2\delta_x^2 + (q'-q)^2\delta_y^2} \right) \right. \\ &\quad \left. \times (\mathbb{C}^2(b_{ll'}) + \mathbb{D}^2(b_{ll'})) \right\}. \end{aligned}$$

Finally, by using the fact that $d_{\text{wc}} = R$ and after substituting (44) and (52) into (35), we get (37). ■

From the Theorem 3.1, we derive the following result. When the UAVs are located on the surface of the sphere, i.e. when $R_{\min} \rightarrow R$, we obtain that

$$\mathbb{C}(b_{ll'}) \rightarrow \frac{1}{6R^2} f'(R) = \cos(b_{ll'}/R)$$

and

$$\mathbb{D}(b_{ll'}) \rightarrow \frac{1}{6R^2} g'(R) = \sin(b_{ll'}/R),$$

where $f'(x)$ and $g'(x)$ are the derivatives of

$$f(x) = (2x^2 - b_{ll'}^2)x \cos \left(\frac{b_{ll'}}{x} \right) - b_{ll'}x^2 \sin \left(\frac{b_{ll'}}{x} \right) - b_{ll'}^3 \text{Si} \left(\frac{b_{ll'}}{x} \right)$$

and

$$g(x) = (2x^2 - b_{ll'}^2)x \sin \left(\frac{b_{ll'}}{x} \right) + b_{ll'}x^2 \cos \left(\frac{b_{ll'}}{x} \right) + b_{ll'}^3 \text{Ci} \left(\frac{b_{ll'}}{x} \right),$$

respectively.

Since $\mathbb{C}^2(b_{ll'}) + \mathbb{D}^2(b_{ll'}) \rightarrow \cos^2(b_{ll'}/R) + \sin^2(b_{ll'}/R) = 1$, the lower bound becomes as given in (53) (shown on top of next page). The quantity Ω_1 in (53) depends on the spacing between the elements of the GS array. We discuss the impact of antenna spacing on the ergodic rate in Section IV. Note that since $\kappa = \mathbb{E} \left\{ \frac{1}{\chi_k} \right\}$, we have that $\kappa \chi_{\text{wc}} < 1$.

B. Zero forcing (ZF) receiver

In this section by assuming that perfect CSI is available at the GS we derive and analyze a lower bound on ergodic

$$S_k^{\text{lb}, \text{MRC}} \rightarrow \Lambda \log_2 \left(1 + \frac{M\rho_u}{\rho_u(K-1) \left(1 + \frac{\Omega_1}{M} \right) + 1 + \frac{\kappa\chi_{\text{wc}}}{\rho_u\rho_p} (1+K\rho_u)} \right), \quad R_{\min} \rightarrow R, \quad (53)$$

where $\Omega_1 = \sum_{l=1}^M \sum_{l'=1, l' \neq l}^M \text{sinc}^2 \left(\frac{2}{\lambda} \sqrt{(p'-p)^2 \delta_x^2 + (q'-q)^2 \delta_y^2} \right)$.

capacity with the ZF receiver. By using the ZF detector, the received signal \mathbf{y} is separated into K streams by multiplying it with $\mathbf{G}^\dagger = (\mathbf{G}^H \mathbf{G})^{-1} \mathbf{G}^H$ as follows

$$\mathbf{r} = \mathbf{G}^\dagger \mathbf{y}.$$

The output of the ZF detector can be written as

$$\mathbf{r} = \mathbf{G}^\dagger (\mathbf{G}(\sqrt{p_u} \odot \mathbf{q}) + \mathbf{n}) = (\sqrt{p_u} \odot \mathbf{q}) + \mathbf{G}^\dagger \mathbf{n}. \quad (54)$$

Since the first and the second terms in (54) are independent of each other, for a given channel matrix \mathbf{G} , the $K \times K$ covariance matrix of \mathbf{r} can be written as

$$\begin{aligned} & \mathbb{E}\{\mathbf{r}\mathbf{r}^H | \mathbf{G}\} \\ &= \mathbb{E}\left\{ ((\sqrt{p_u} \odot \mathbf{q}) + \mathbf{G}^\dagger \mathbf{n}) ((\sqrt{p_u} \odot \mathbf{q}) + \mathbf{G}^\dagger \mathbf{n})^H \right\} \\ &= \mathbb{E}\left\{ (\sqrt{p_u} \odot \mathbf{q})(\sqrt{p_u} \odot \mathbf{q})^H \right\} + \mathbb{E}\left\{ \mathbf{G}^\dagger \mathbf{n} \mathbf{n}^H (\mathbf{G}^\dagger)^H \right\} \\ &= \text{diag}(p_{u1}, \dots, p_{uK}) + \mathbf{G}^\dagger \mathbb{E}\{\mathbf{n} \mathbf{n}^H\} (\mathbf{G}^\dagger)^H \\ &= \text{diag}(p_{u1}, \dots, p_{uK}) + \mathbf{G}^\dagger \mathbf{I}_M (\mathbf{G}^\dagger)^H \\ &= \text{diag}(p_{u1}, \dots, p_{uK}) + (\mathbf{G}^H \mathbf{G})^{-1}, \end{aligned}$$

where we used the facts that $\mathbb{E}\{(\sqrt{p_u} \odot \mathbf{q})(\sqrt{p_u} \odot \mathbf{q})^H\} = \text{diag}(p_{u1}, \dots, p_{uK})$, $\mathbb{E}\{\mathbf{n} \mathbf{n}^H\} = \mathbf{I}_M$, and $\mathbf{G}^\dagger (\mathbf{G}^\dagger)^H = (\mathbf{G}^H \mathbf{G})^{-1}$.

The post processing SINR for the k -th UAV is $\gamma_k^{\text{ZF}} = \frac{p_{uk}}{\left[(\mathbf{G}^H \mathbf{G})^{-1} \right]_{kk} \left[\text{adj}(\mathbf{G}^H \mathbf{G}) \right]_{kk}}$. Since we know that $\left[(\mathbf{G}^H \mathbf{G})^{-1} \right]_{kk} = \frac{1}{\det(\mathbf{G}^H \mathbf{G})} \left[\text{adj}(\mathbf{G}^H \mathbf{G}) \right]_{kk}$, we can write

$$\gamma_k^{\text{ZF}} = \frac{p_{uk} \det(\mathbf{G}^H \mathbf{G})}{\left[\text{adj}(\mathbf{G}^H \mathbf{G}) \right]_{kk}}.$$

By the convexity of $\log_2(1 + \frac{1}{t})$ and Jensen's inequality, a lower bound on the achievable uplink rate using ZF receiver can be obtained as

$$\begin{aligned} S_k^{\text{ZF}} &\geq S_k^{\text{lb}, \text{ZF}} = \Lambda \log_2 \left(1 + \left(\mathbb{E} \left\{ \frac{1}{\gamma_k^{\text{ZF}}} \right\} \right)^{-1} \right) \quad (55) \\ &= \Lambda \log_2 \left(1 + \left(\mathbb{E} \left\{ \frac{\left[\text{adj}(\mathbf{G}^H \mathbf{G}) \right]_{kk}}{p_{uk} \det(\mathbf{G}^H \mathbf{G})} \right\} \right)^{-1} \right), \end{aligned}$$

where $p_{uk} \leq p_u$.

The expectation in (55) has to be taken over the distances d_k , the elevation angles θ_k , and the azimuth angles ϕ_k for all $k \in \{1, 2, \dots, K\}$. Since it is difficult to find the expectation for general K UAVs scenario, we analyze the lower bound for

$K = 2$. In this case, the determinant of $\mathbf{G}^H \mathbf{G}$ can be obtained as

$$\begin{aligned} \det(\mathbf{G}^H \mathbf{G}) &= \|\mathbf{g}_1\|^2 \|\mathbf{g}_2\|^2 - (\mathbf{g}_1^H \mathbf{g}_2)(\mathbf{g}_2^H \mathbf{g}_1) \\ &= M^2 \beta_1 \beta_2 \chi_1 \chi_2 \\ &\quad - \beta_1 \beta_2 \chi_1 \chi_2 \left(M + \sum_{l=1}^M \sum_{\substack{l'=1, \\ l' \neq l}}^M e^{i \frac{2\pi}{\lambda} (d_{1l} - d_{1l'} - d_{2l} + d_{2l'})} \right). \end{aligned}$$

We have also $[\text{adj}(\mathbf{G}^H \mathbf{G})]_{kk} = \|\mathbf{g}_{3-k}\|^2 = M \beta_{3-k} \chi_{3-k}$ for $k = 1, 2$. Therefore, by applying (28), the expectation in (55) is obtained as

$$\begin{aligned} & \mathbb{E} \left\{ \frac{[\text{adj}(\mathbf{G}^H \mathbf{G})]_{kk}}{p_{uk} \det(\mathbf{G}^H \mathbf{G})} \right\} = \mathbb{E} \left\{ \frac{M \beta_1 \beta_2 \chi_1 \chi_2}{\rho_u \det(\mathbf{G}^H \mathbf{G})} \right\} \quad (56) \\ &= \frac{1}{\rho_u} \mathbb{E} \left\{ \left(M - \left(1 + \frac{1}{M} \sum_{l=1}^M \sum_{\substack{l'=1, \\ l' \neq l}}^M e^{i \frac{2\pi}{\lambda} (d_{1l} - d_{1l'} - d_{2l} + d_{2l'})} \right) \right)^{-1} \right\}. \end{aligned}$$

Finally, by substituting (56) into (55), we get the lower bound as given in (57) (shown on top of next page).

IV. ERGODIC RATE PERFORMANCE WITH OPTIMAL ANTENNA SPACING

In this section we analyze the ergodic rate performance with optimal antenna spacing for ULA and URA structures.

A. Optimal antenna spacing

Uniform linear array: For an ULA, i.e. $M_y = 1$, since the zero crossings of the $\text{sinc}(u)$ are at non-zero integer multiples of u , the quantity Ω (as given in (38)) is zero whenever $\delta_x = n \frac{\lambda}{2}$, $n = 1, 2, \dots, \lfloor \frac{2R_{\min}}{\lambda(M-1)} \rfloor$ (Here the maximum value of n is obtained from (36)). Therefore, for an ULA, the optimal antenna spacing for maximizing the ergodic rate is

$$\delta_x^* = n \frac{\lambda}{2}, \quad n = 1, 2, \dots, \left\lfloor \frac{2R_{\min}}{\lambda(M-1)} \right\rfloor. \quad (58)$$

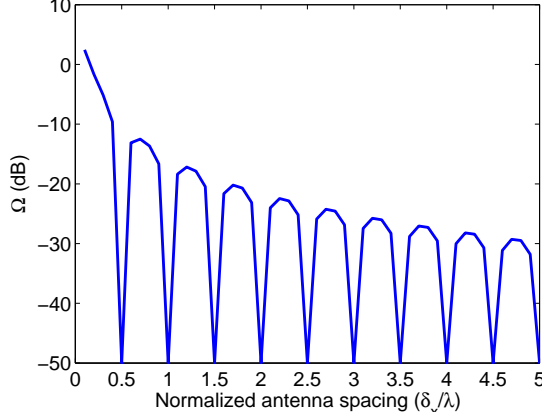
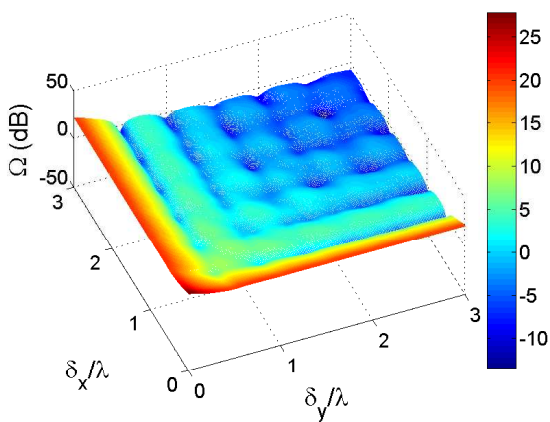
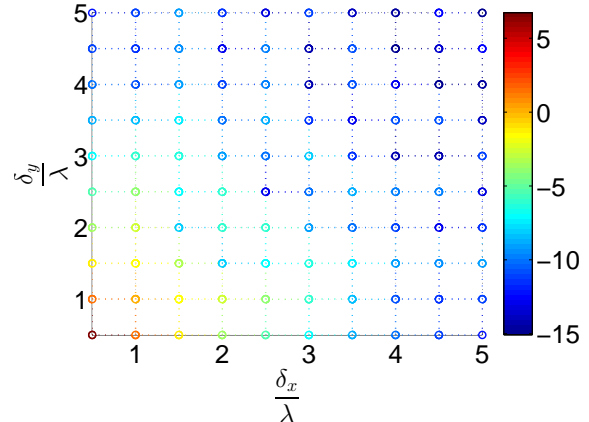
Interestingly, the result in (58) is the same as in the case of isotropic scattering [36]. Figure 5(a) shows the quantity Ω as a function of antenna spacing-wavelength ratio on x -axis (i.e. $\frac{\delta_x}{\lambda}$) for $M_x = 50$ and $M_y = 1$.

Uniform rectangular array: For an URA, the sinc function in (38) will not be vanishing as the arguments will not be an integer for cross diagonal elements. However, we observe that there are local minimas at

$$(\delta_x, \delta_y) \approx \left(n \frac{\lambda}{2}, m \frac{\lambda}{2} \right), \quad (59)$$

where n and m are positive integers. This can be seen from Figure 5(b) which shows Ω as a function of the antenna

$$S_k^{\text{lb}, \text{ZF}} = \Lambda \log_2 \left(1 + \rho_u \left[\mathbb{E} \left\{ \left(M - \left(1 + \frac{1}{M} \sum_{l=1}^M \sum_{l'=1, l' \neq l}^M e^{i \frac{2\pi}{\lambda} (d_{1l} - d_{1l'} - d_{2l} + d_{2l'})} \right) \right)^{-1} \right\} \right]^{-1} \right), \quad k = 1, 2. \quad (57)$$

(a) Ω (dB) for $M_x = 50$, $M_y = 1$ (b) Ω (dB) for $M_x = 5$, $M_y = 5$ (c) Ω (dB) for $M_x = 5$, $M_y = 5$ Fig. 5. Ω as a function of antenna spacing-wavelength ratio for $\lambda = 12.5$ cm and $R = 500$ m.

spacing-wavelength ratio on x -axis ($\frac{\delta_x}{\lambda}$) and y -axis ($\frac{\delta_y}{\lambda}$). Note that for a given inner radius of the spherical shell R_{\min} as in (36), the values of n and m are limited by the maximum allowable aperture size of the array, i.e.

$$(M_x - 1)^2 n^2 + (M_y - 1)^2 m^2 < \frac{4R_{\min}^2}{\lambda^2}.$$

Furthermore, numerical observations show that Ω is close to zero whenever $n \geq M_y$ and $m \geq M_x$. For instance, with $n = M_y$ and $m = M_x$, we observe that $\Omega \approx 0.053$. This can be seen from Figure 5(c) which shows only the values of Ω at (59). Therefore, for an URA, an appropriate choice of antenna spacing for maximizing the ergodic rate could be

$$\begin{aligned} (\delta_x^*, \delta_y^*) &= \left(n \frac{\lambda}{2}, m \frac{\lambda}{2} \right), \quad n \geq M_y, \quad m \geq M_x, \\ (M_x - 1)^2 n^2 + (M_y - 1)^2 m^2 &< \frac{4R_{\min}^2}{\lambda^2}. \end{aligned} \quad (60)$$

B. Achievable rate performance with optimal antenna spacing

MRC receiver: With the optimal antenna spacing as given in (58) and (60), by employing MRC receiver at the GS, when $R_{\min} \rightarrow R$, from (53) we obtain that

$$\begin{aligned} S_k^{\text{lb}, \text{MRC}} &\quad (61) \\ &= \begin{cases} \Lambda \log_2 \left(1 + \frac{M \rho_u}{\rho_u (K-1) + 1 + \frac{\kappa_{\text{Xwc}}}{\rho_u \rho_p} (1 + K \rho_u)} \right), & \text{for ULA,} \\ \Lambda \log_2 \left(1 + \frac{M \rho_u}{\rho_u (K-1) \left(1 + \frac{\Omega_{\text{URA}}}{M} \right) + 1 + \frac{\kappa_{\text{Xwc}}}{\rho_u \rho_p} (1 + K \rho_u)} \right), & \text{for URA,} \end{cases} \end{aligned}$$

where $\Omega_{\text{URA}} = \sum_{l=1}^M \sum_{l'=1, l' \neq l}^M \text{sinc}^2 \left(\sqrt{(p' - p)^2 n^2 + (q' - q)^2 m^2} \right)$, $l = (q-1)M_x + p$, $p \in \{1, 2, \dots, M_x\}$, $q \in \{1, 2, \dots, M_y\}$, $n \geq M_y$, $m \geq M_x$, and $(M_x - 1)^2 n^2 + (M_y - 1)^2 m^2 < \frac{4R_{\min}^2}{\lambda^2}$.

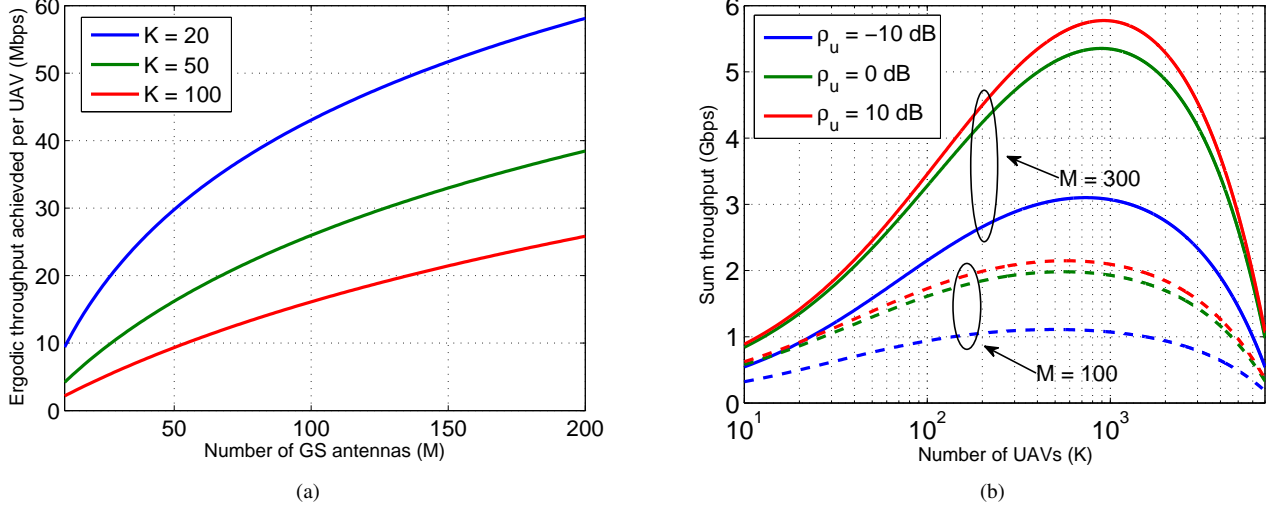


Fig. 6. (a) Ergodic throughput achieved per UAV vs. Number of GS antennas (M) with the MRC receiver for $\rho_u = 0$ dB, $\rho_p = 10$ dB, $\tau_{\text{dl}} = \frac{T_{\text{len}}}{8}$, $B = 20$ MHz, $B_c = 3$ MHz, $f_c = 2.4$ GHz, and $v_{\max} = 20$ m/s. (b) Sum throughput (in Gbps) vs. Number of UAVs for $\rho_p = 10$ dB and different values of ρ_u and M .

For an ULA, the sum rate achieved by the K UAVs is then

$$\begin{aligned} S_{\text{sum},K}^{\text{MRC}} &= \sum_{k=1}^K S_k^{\text{lb,MRC}} \\ &= \Lambda K \log_2 \left(1 + \frac{M \rho_u}{\rho_u (K-1) + 1 + \frac{\kappa \chi_{\text{wc}}}{\rho_u \rho_p} (1 + K \rho_u)} \right). \end{aligned} \quad (62)$$

It can be observed from (61) that for a given K , the rate grows unbounded with M . If we define ergodic throughput, $Q = B \cdot S$ bits/sec (where S is the ergodic rate in bits/sec/Hz and B is the system bandwidth in Hz), it can be derived from (61) that when $R_{\min} \rightarrow R$, the minimum number of antennas required to support a target data rate of Q_{tar} (bits/s) is

$$M_{\text{req}} = \left((K-1) + \frac{1}{\rho_u} + \frac{\kappa \chi_{\text{wc}}}{\rho_u^2 \rho_p} (1 + K \rho_u) \right) \left(2^{\frac{Q_{\text{tar}}}{\Lambda B}} - 1 \right). \quad (63)$$

Figure 6(a) shows the ergodic throughput achieved per UAV (Q) versus the number of GS antennas (M) for varying number of simultaneously communicating UAVs when $\kappa \chi_{\text{wc}} = 1$, $\tau_{\text{dl}} = \frac{T_{\text{len}}}{8}$, $\rho_u = 0$ dB, $\rho_p = 10$ dB, $B = 20$ MHz, $B_c = 3$ MHz, $f_c = 2.4$ GHz, and $v_{\max} = 20$ m/s. It can be seen that, in order to support the data rate of 20 Mbps, for $K = 20, 50$, and 100 UAVs the number of antenna elements required is approximately equal to 27, 68, and 136, respectively. With the same parameters as in the previous case, Figure 6(b) shows the sum throughput ($Q_{\text{sum}} = K \cdot B \cdot S$) versus the number of UAVs (K) for different values of data SNR (ρ_u) and varying number of GS antennas. For a given ρ_u , the sum throughput increases up to a certain value of K and decreases with further increase in K . This is because the pre-log term decreases with the number of UAVs due to the finite number of symbols in a coherence interval.

ZF receiver: With ZF receiver, since it is difficult to calculate the expectation in (57), we provide the asymptotic

result. For large M , we observed that the term $\frac{1}{M} \sum_{l=1}^M \sum_{l'=1, l' \neq l}^M e^{i \frac{2\pi}{\lambda} (d_{1l} - d_{1l'} - d_{2l} + d_{2l'})}$ in (57) tends to zero, i.e.

$$\frac{S_k^{\text{lb,ZF}}}{\Lambda \log_2 (1 + M \rho_u)} \rightarrow 1, \quad k = 1, 2. \quad (64)$$

Note that when compared to MRC receiver, additional sum-rate performance gains at medium and high SNR regime are possible with the ZF receiver [13]. This is a topic for future work.

It is interesting to see from (61) and (64) that only by increasing the number of antenna elements at the GS, one can increase the uplink capacity of UAV communication system without increasing the UAV's transmit power.

Power scaling law: Consider a case with the perfect CSI (i.e. $\rho_p \rightarrow \infty$). If the UAV's transmit power is scaled down according to $\rho_u = \frac{\varepsilon_u}{M}$, where ε_u is fixed, then for large M , the lower bounds in (61) and (64) (i.e. $S_k^{\text{lb,MRC}}$ and $S_k^{\text{lb,ZF}}$) tend to $\Lambda \log_2 (1 + \varepsilon_u)$. This implies that, with finite K , when M grows large, each UAV obtains the same rate performance as in the single UAV case.

V. IMPACT OF POLARIZATION MISMATCH AND ANTENNA PATTERN ON THE LINK RELIABILITY

Since each UAV performs instantaneous power control to maintain an equal data SNR ρ_u according to (24), at the GS, the received power on the coherence channel bandwidth B_c remains the same for all drones (i.e. $\rho_u N_0 B_c$ (W), where N_0 is the noise spectral density (i.e. $N_0 = k_B T 10^{\mathcal{F}/10} \approx 2 \times 10^{-20}$ J, where $k_B = 1.38 \times 10^{-23}$ J/K, $T = 290$ K, and the receiver noise figure $\mathcal{F} = 7$ dB). Therefore, if the distance between the GS and the UAV location is much larger than the GS array's aperture size (i.e. $d_{kl} \approx d_k, \forall l$), for given positions

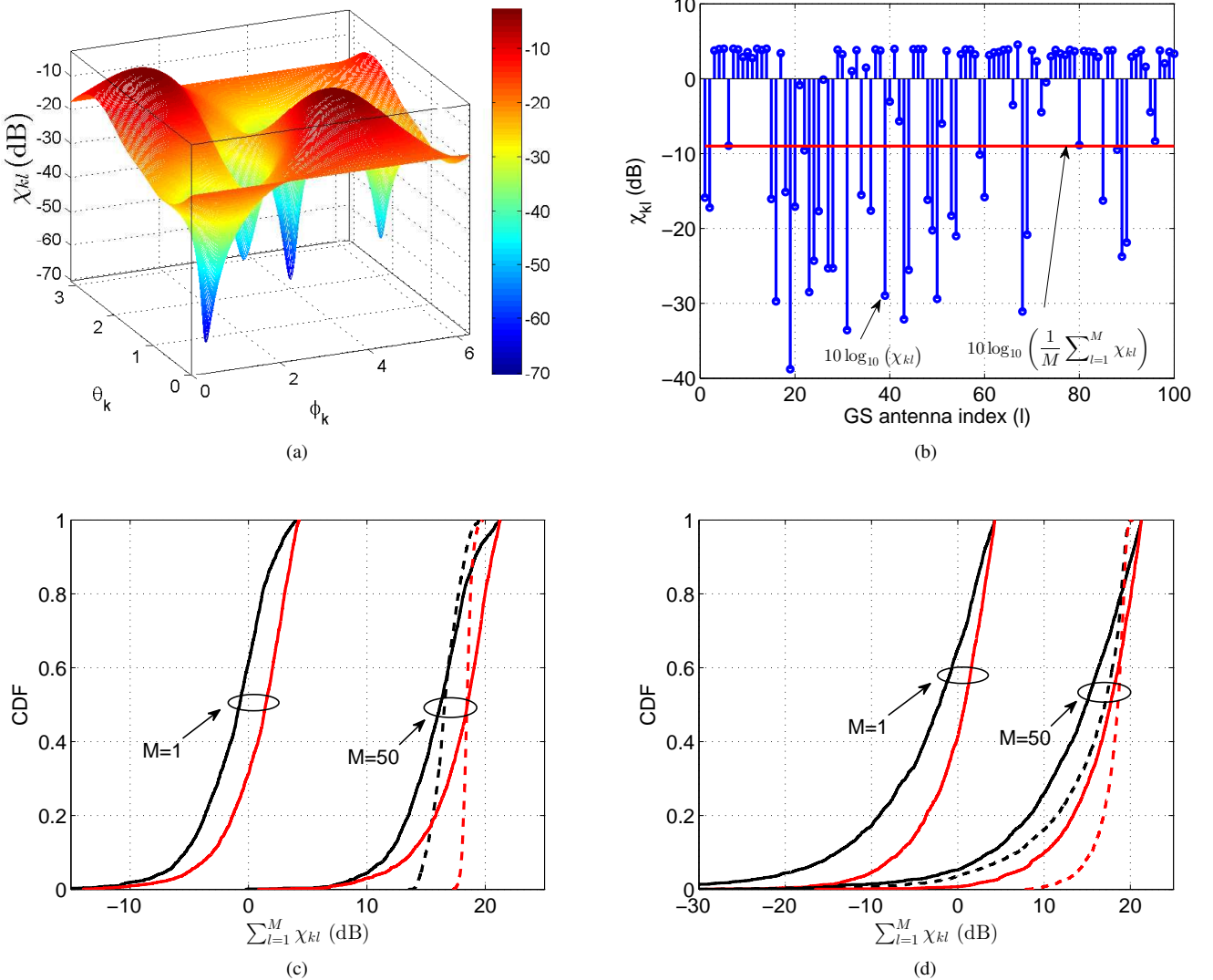


Fig. 7. (a) Effective gain (including antenna gain and polarization mismatch loss) with identically oriented GS array elements for $\lambda = 12$ cm, $d_k = 100$ m, $\delta_x = \frac{\lambda}{2}$ m, $d_{\text{len}} = \frac{\lambda}{2}$ m with $E_\theta^l = \frac{1}{\sqrt{2}}$, $E_\theta'^k = \frac{i}{\sqrt{2}}$ and $E_\psi^l = E_\psi'^k = \frac{1}{\sqrt{2}}$. (b) Effective gain with arbitrarily oriented GS array elements for $M_x = 100$, $M_y = 1$, $\theta_k = \frac{\pi}{3}$, $\phi_k = \pi$. (c) CDF of $(\sum_{l=1}^M \chi_{kl})$ for $M_x = 50$, $M_y = 1$ and $E_\theta^l = \frac{1}{\sqrt{2}}$, $E_\psi^l = \frac{i}{\sqrt{2}}$, $E_\theta'^k = \frac{1}{\sqrt{2}}$, $E_\theta'^k = \frac{-i}{\sqrt{2}}$ (circularly polarized antenna elements; solid lines: identically oriented GS elements, dashed lines: pseudo-randomly oriented GS elements, red lines: isotropic antenna pattern, black lines: dipole antenna pattern). (d) CDF of $(\sum_{l=1}^M \chi_{kl})$ for $M_x = 50$, $M_y = 1$ and $E_\theta^l = 1$, $E_\psi^l = 0$, $E_\theta'^k = 1$, $E_\theta'^k = 0$ (linearly polarized antenna elements).

of GS and k -th UAV, the required transmit power per data symbol is calculated from (24) as

$$p_{uk} = \rho_u N_0 B_c \left(\frac{4\pi d_k}{\lambda} \right)^2 \frac{1}{\frac{1}{M} \sum_{l=1}^M \chi_{kl}} \quad (\text{W}).$$

Note that the quantity χ_{kl} consists of polarization mismatch loss factors, and transmit and receive antenna patterns. The required pilot power is obtained using (22) as

$$p_p = \rho_p N_0 B_c \left(\frac{4\pi d_{\text{wc}}}{\lambda} \right)^2 \frac{1}{\chi_{\text{wc}}} \quad (\text{W}).$$

Then the instantaneous uplink power (in W) required by the k -th UAV over bandwidth of B Hz is

$$\begin{aligned} p_{uk,\text{Tot}} &= \frac{B}{B_c} \left(\Lambda p_{uk} + \left(\frac{K}{T_{\text{len}}} \right) p_p \right) \\ &= B N_0 \left(\frac{4\pi}{\lambda} \right)^2 \\ &\times \left(\Lambda \rho_u d_k^2 \frac{1}{\frac{1}{M} \sum_{l=1}^M \chi_{kl}} + \left(\frac{K}{T_{\text{len}}} \right) \rho_p d_{\text{wc}}^2 \frac{1}{\chi_{\text{wc}}} \right). \end{aligned} \quad (65)$$

In this section, to show the effect of the polarization mismatch loss and antenna patterns we analyze the effective gain $\sum_{l=1}^M \chi_{kl}$ for the randomly and uniformly distributed UAV positions within a spherical shell with inner radius $R_{\min} = 20$ m

and outer radius $R = 500$ m. The uniformly distributed UAV locations inside a spherical volume are obtained using the procedure as detailed in [37, p.130]. We consider an ULA with antenna spacing $\delta_x = \frac{\lambda}{2} = 6.25$ cm ($f_c = 2.4$ GHz). The roll, pitch, and yaw angles both at the GS and at the UAV are uniformly distributed in the interval $[-\frac{\pi}{2}, \frac{\pi}{2}]$, $[-\frac{\pi}{2}, \frac{\pi}{2}]$, and $[0, \frac{\pi}{2}]$, respectively.

When all GS array elements are identically oriented (i.e. $\mathbf{R}_{kl}^{\times,+} = \mathbf{I}_3$ and $\chi_{kl} \approx \chi_k, \forall l$), with an arbitrarily chosen roll, pitch, and yaw angles, Figure 7(a) shows the effective gain (χ_{kl}) for varying elevation and azimuth angles with $E_\theta^l = \frac{1}{\sqrt{2}}, E_\psi^l = \frac{i}{\sqrt{2}}, E_\theta'^k = E_\psi'^k = \frac{1}{\sqrt{2}}$. It can be observed that the gain is very low at certain orientation angles (below -50 dB in some cases). This implies that if all the GS antenna array elements are identically oriented, most likely the signal will be lost for certain positions and orientation of the UAV.

For example, consider the following parameters: $K = 20$, $\rho_u = 10$ dB, $\rho_p = 10$ dB, $\tau_{dl} = \frac{T_{len}}{8}$, $B = 20$ MHz, $B_c = 3$ MHz, $f_c = 2.4$ GHz, and $v_{max} = 20$ m/s. If $d_k = 400$ m, since $d_{wc} = R$, the total transmit power required by the UAV is $p_{uk,Tot} = \frac{9.2 \times 10^{-3}}{\frac{1}{M} \sum_{l=1}^M \chi_{kl}} + \frac{2.3 \times 10^{-5}}{\chi_{wc}}$ W. Now the required uplink power depends on the relative orientation of the GS and UAV antenna elements. When all GS elements are identically oriented, as a result of low gain as shown in Figure 7(a), the required uplink power will be very high. For example, if we consider $\frac{1}{M} \sum_{l=1}^M \chi_{kl} = -40$ dB and $\chi_{wc} = -50$ dB, the required transmit power is $p_{uk,Tot} \approx 94$ W. Since the UAV's power supply is limited in practice, the outage probability (as defined in (26)) will be high. This situation can be avoided by arbitrarily orienting the GS array elements.

When all GS array elements are arbitrarily oriented, Figure 7(b) shows the effective gain experienced by an individual antenna element for $M_x = 100$, $M_y = 1$, $\theta_k = \frac{\pi}{3}$, and $\phi_k = \pi$. It can be observed that not all elements experience low gain. As a result, the nulls as shown in Figure 7(a) can be canceled out due to polarization diversity. For example, from Figure 7(b), it can be observed that the average gain (i.e. $\frac{1}{M} \sum_{l=1}^M \chi_{kl}$) is approximately equal to -8 dB.

Figure 7(c) shows the CDF of $(\sum_{l=1}^M \chi_{kl})$ with identical and pseudo-randomly oriented GS elements for $M_x = 1, 50, M_y = 1$, and $E_\theta^l = \frac{1}{\sqrt{2}}, E_\psi^l = \frac{i}{\sqrt{2}}, E_\theta'^k = \frac{1}{\sqrt{2}}, E_\theta'^k = \frac{-i}{\sqrt{2}}$ (circularly polarized cross-dipoles both at the GS and at the UAV). The solid and dashed lines denote the gain values with identical and pseudo-randomly oriented GS elements, respectively. The black lines represent the gain values with an omni-directional antenna pattern (only in the azimuthal direction) while the red lines represent the gain values power with a hypothetical isotropic antenna pattern (i.e. the gain is assumed to be 1 for all θ_k and ϕ_k). Similarly, Figure 7(d) shows the CDF of $(\sum_{l=1}^M \chi_{kl})$ for $M_x = 50, M_y = 1$ and $E_\theta^l = 1, E_\psi^l = 0, E_\theta'^k = 1, E_\theta'^k = 0$ (linearly polarized dipoles both at the GS and at the UAV).

From Figures 7(c) and 7(d) we make the following observations:

- By increasing the number of antennas from 1 to 50, the gain is increased by a factor of 50 (≈ 17 dB).
- Employing linearly polarized antennas either at the GS or

UAV results in lower gain. Irrespective of the orientation of the GS array elements, almost always the gain varies between -30 and 21 dB.

- Circularly polarized cross-dipoles perform far better than the linearly polarized dipoles. Consider a threshold value of 10 dB gain. When GS elements are identically oriented (solid lines), the probability of experiencing gain below 10 dB (This corresponds to $\frac{1}{M} \sum_{l=1}^M \chi_{kl} \approx -7$ dB) is 0.045 for circularly polarized cross-dipoles and 0.26 for linearly polarized dipoles. This is due to the nulls as observed in Figure 7(a). On the other hand, when the GS elements are pseudo-randomly oriented (dashed lines), the probability is zero and 0.16 for circular polarized and linearly polarized dipoles, respectively.
- With circularly polarized cross-dipoles, the value of χ_{wc} is around -17 dB for identical orientation and -3.5 dB for arbitrary orientation. This will significantly reduce the uplink power. For example, if we consider $\frac{1}{M} \sum_{l=1}^M \chi_{kl} = -12$ dB and $\chi_{wc} = -20$ dB, the required transmit power is $p_{uk,Tot} = 0.15$ W. This means that, using arbitrarily oriented GS elements, it is possible to achieve 100% coverage with very low uplink transmit power. As it has been seen earlier, this is not possible with identically oriented array elements.
- Since the cross-dipole provides quasi-isotropic gain pattern, the gain difference with the isotropic antenna pattern is only around 3 dB. By adding third dipole, the difference in gain can be further reduced.

The above results clearly suggest that by using simple cross-dipole antenna elements with circular polarization both at the GS (with arbitrary orientation) and at the UAV one can achieve the link reliability requirements of the UAV networks.

VI. SURVEILLANCE USE CASE

Consider a scenario with $K = 20$ drones each equipped with a camera (with resolution of $r_{py} \times r_{px}$ [pixel], $r_{py} > r_{px}$) scanning a particular geographical region with an area A and transmitting images or streaming videos to the GS located at the origin (see Figure 8(a)). An ULA with $M_x = 100$ elements is located along the x -axis. The GS array elements are arbitrarily oriented and the UAV's dipoles are oriented along the x - and z -axes. Let $X_1 = -1000, X_2 = 2000, Y_1 = 2000$ and $Y_2 = 6000$. The total area is $A = 3 \text{ km} \times 4 \text{ km}$ and the area covered by each drone is $A_{\text{drone}} = \frac{A}{K} = 600 \text{ m} \times 1000 \text{ m}$. For simplicity of the analysis, we assume that, at certain altitude H m, all 20 drones move simultaneously at constant speed v m/s along their trajectory as shown in Figure 8(b). Let the starting position of the k -th drone be $(X_1 + (i-1)\frac{(X_2-X_1)}{5}, Y_1 + j\frac{(Y_2-Y_1)}{4}, H)$, $k = 5(j-1)+i$, $i = 1, \dots, 5$, $j = 1, \dots, 4$.

When $H = 100$ m, $M_x = 100$, $M_y = 1$, $f_c = 2.4$ GHz, $B = 20$ MHz, $B_c = 3$ MHz, $\rho_u = 10$ dB, $\rho_p = 20$ dB, $v = 30$ m/s, and $E_\theta^l = \frac{i}{\sqrt{2}}, E_\psi^l = \frac{i}{\sqrt{2}}, E_\theta'^k = \frac{i}{\sqrt{2}}, E_\theta'^k = \frac{i}{\sqrt{2}}$, Figures 9(a) and 9(b) show the instantaneous throughput achieved by the four corner drones (with index 1, 5, 17, and 20) each drone covers colored regions in Figure 8(a)) with antenna spacing $\delta_x = \frac{\lambda}{2} = 6.25$ cm and $\delta_x = 5\lambda = 0.625$

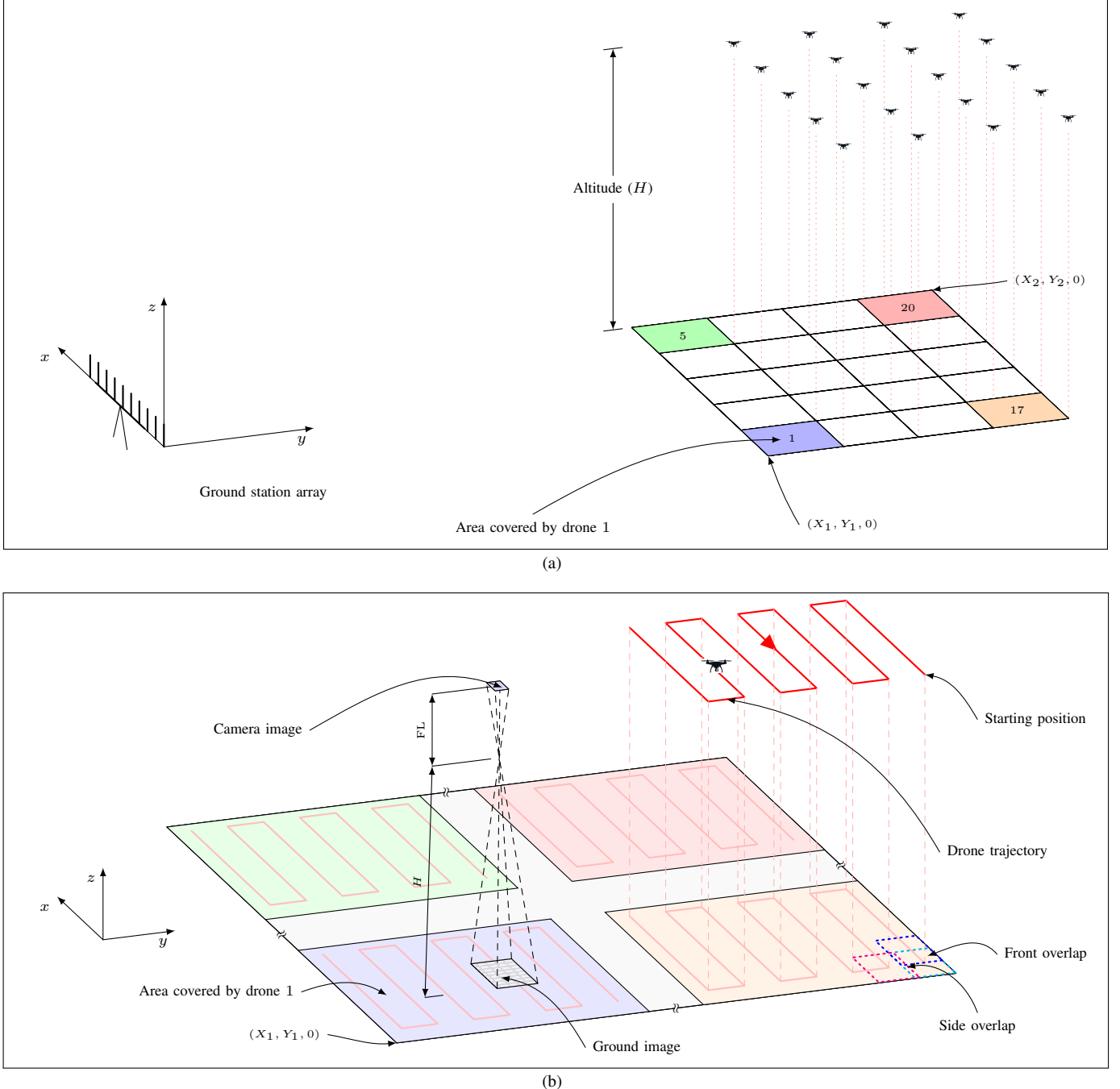


Fig. 8. (a) Drone surveillance scenario. (b) Enlarged version of Figure 8(a) with camera's geometry and drone's trajectory (The line colors correspond to the colored region as shown in 8(a), Blue: Drone 1, Green: Drone 5, Orange: Drone 17, Red: Drone 20).

m, respectively⁵. Due to the movement of the drones, the cumulative interference from the other $K - 1 = 19$ drones fluctuates as the azimuth and elevation angles vary with time which results in varying instantaneous throughput. With increased antenna spacing $\delta_x = 5\lambda$, the capacity fluctuates more frequently due to increased resolving capability of the GS array. The instantaneous transmit powers of the drones obtained from (65) are shown in Figure 9(c). The pilot power is chosen based on the worst-case values of the distance (6325 m at (X_2, Y_2, H)) and $\chi_{wc} = -10$ dB. Further, with $\delta_x = \frac{\lambda}{2}$, when increasing the number of GS antennas by a factor of

10 (i.e. M_x is changed from 100 to 1000) and reducing the transmit power values (as shown in Figure 9(c)) by a factor of 10, the instantaneous throughput performance is shown in Figure 9(d).

⁵From the received signal as given in (29), the instantaneous uplink throughput achieved by the k -th UAV can be expressed as $S_k^{\text{inst}} = AB \log_2 \left(1 + \frac{p_{uk} |\hat{\mathbf{g}}_k^H \mathbf{g}_k|^2}{\sum_{j=1, j \neq k}^K p_{uj} |\hat{\mathbf{g}}_k^H \mathbf{g}_j|^2 + |\hat{\mathbf{g}}_k|^2} \right)$ (bits/s).

⁶GSD is the distance between the centers of two neighbouring pixels measured on the ground while PS is the distance between two pixels measured on the camera's sensor. Depending on the mission, the target GSD varies from a few centimeters to a few meters [38], [39].

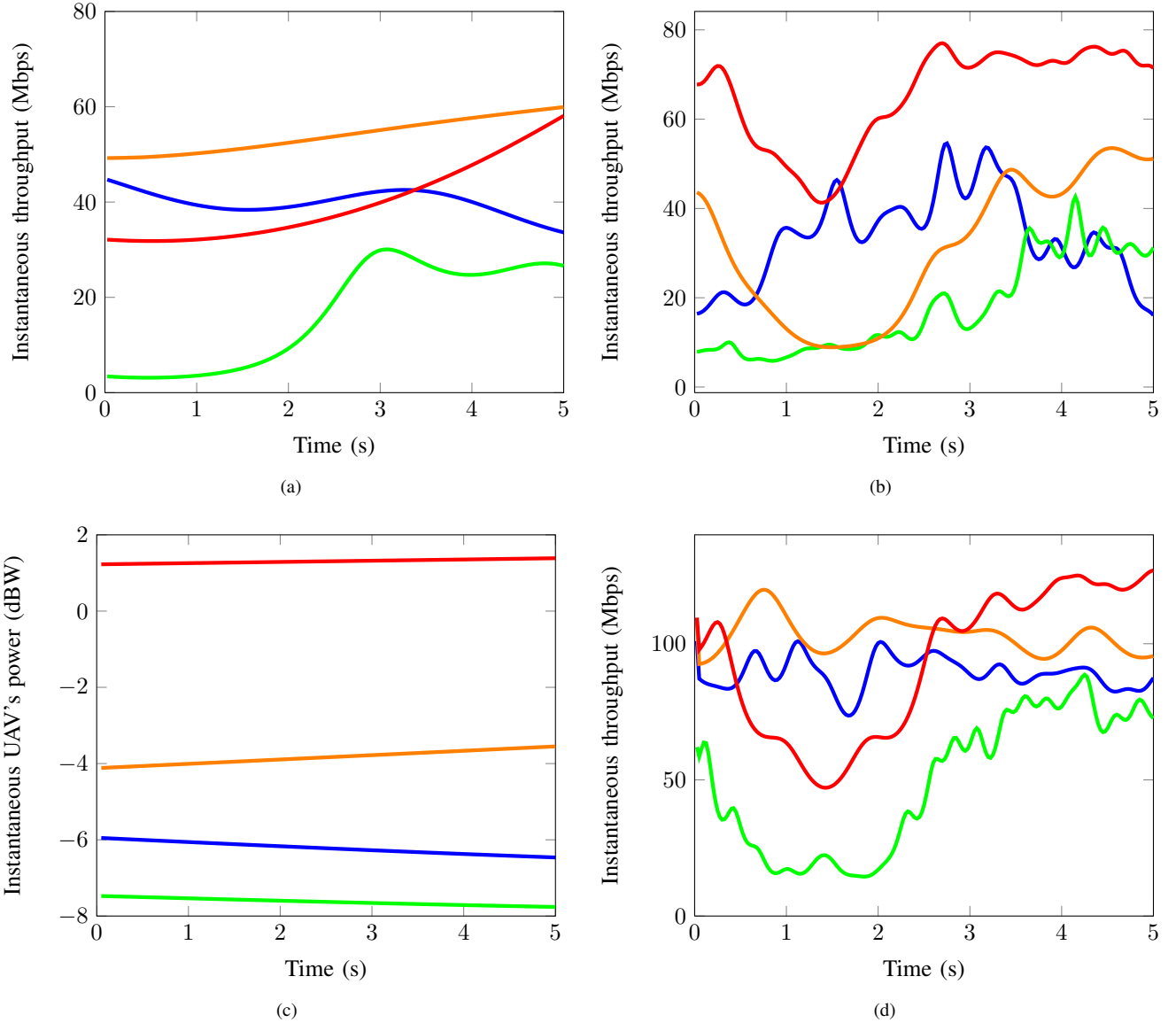


Fig. 9. (a) Instantaneous throughput achieved by the four corner drones for $\delta_x = \frac{\lambda}{2}$ and $M_x = 100$. (b) Instantaneous throughput achieved for $\delta_x = 5\lambda$ and $M_x = 100$. (c) Instantaneous transmit power of the four corner drones. (d) Instantaneous throughput achieved for $\delta_x = \frac{\lambda}{2}$ and $M_x = 1000$ (Note that the number of antennas in increased by a factor of 10 and the uplink power is reduced by a factor of 10.)

In surveillance missions, the main requirement is to scan the region of interest with certain spatial resolution or ground sampling distance (GSD). As illustrated in Figure 8(b), for a given target GSD and the dimensions of the camera sensor, the drones have to fly at an altitude of $H = \frac{\text{GSD} \times \text{FL}}{\text{PS}}$ m (where ‘PS’ is the camera sensor’s pixel size and ‘FL’ is the focal length⁶). The area covered by a camera image is $A_{\text{image}} = r_{px} \cdot r_{py} \cdot \text{GSD}^2$. If $\text{FL} = 5 \times 10^{-3}$ m and $\text{PS} = 2.3 \times 10^{-6}$ m [38, Ch.4], for $\text{GSD} = 2 \times 10^{-2}$, 2×10^{-1} , and 1 m, the altitudes are approximately equal to 44, 435, and 2174 m, respectively. When $r_{py} \times r_{px} = 2664 \times 1496$, the corresponding area covered by a camera image is approximately 53.3×30 , 533×300 , and 2664×1496 m², respectively. Let b be the number of bits per pixel generated by the camera’s sensor and CR be the compression ratio. Then the number of bits generated by an image is $D_{\text{image}} = \frac{r_{px} \cdot r_{py} \cdot b}{\text{CR}}$.

We assume that the camera is oriented with the sensor width (long dimension) parallel to the flight direction. Let ‘OL_y’ and ‘OL_x’ be the front and side image overlap, respectively, required by the mission (see Figure 8(b)). The time between two consecutive images is $t = \frac{r_{py} \cdot \text{GSD} \cdot (1 - \text{OL}_y)}{v}$, where v is the drone speed. Then, for image transmission, the data rate required per drone is

$$Q_{\text{image}} = \frac{D_{\text{image}}}{t} = \frac{r_{px} \cdot b \cdot v}{\text{GSD} \cdot \text{CR} \cdot (1 - \text{OL}_y)} \text{ (bits/sec)}. \quad (66)$$

The sum throughput required by K drones is $Q_{\text{image}}^{\text{sum}} = K \times Q_{\text{image}}$ (bits/sec). For video transmission, the sum throughput requirement is

$$Q_{\text{video}}^{\text{sum}} = K \times \frac{r_{px} \cdot r_{py} \cdot b \cdot \text{FPS}}{\text{CR}} \text{ (bits/sec)}, \quad (67)$$

where FPS is the number of frames per second.

TABLE I

DATA RATE REQUIREMENTS FOR IMAGE TRANSMISSION ($K = 20$,
 $r_{py} \times r_{px} = 2664 \times 1496$, $b = 24$, $OL_y = 70\%$)

GSD →	2 cm	5 cm	20 cm
Drone speed $v \rightarrow$	20 m/s	30 m/s	30 m/s
Q_{image} (Uncompressed)	120 Mbps	72 Mbps	18 Mbps
$Q_{\text{image}}^{\text{sum}}$ (Uncompressed)	2.4 Gbps	1.44 Gbps	360 Mbps
M_{req} (Uncompressed)	2195	313	20
M_{req} (Compressed, CR = 2 : 1)	187	61	9

Table I shows the data rate requirements (from (66)) for image transmission with different target GSDs and drone speeds when $K = 20$, $r_{py} \times r_{px} = 2664 \times 1496$, $b = 24$ bits/pixel, and $OL_y = 70\%$. Similarly, the data rate requirements for compressed video transmission with different camera resolutions and frame rates are shown in Table II. Massive MIMO technology can meet this high-throughput, reliable simultaneous communication requirement of UAV swarm by employing the number of antennas (M_{req}) as given in Tables I and II. The lower bound derived as given in (35) is the average value of the instantaneous capacities shown in Figures 9(a) and 9(b). As discussed earlier, since we apply channel inversion power control, for the considered trajectory of the drones in this use case, the ergodic rate expression will be the same as (37) except the quantity Ω . Since Ω decays with antenna spacing, it can be made close to zero by appropriately selecting the antenna spacing: δ_x and δ_y . Therefore, by assuming $\Omega = 0$, the values of number of GS antennas (M_{req}) as shown in Tables I and II are calculated using (34), (63), and (66) for the following parameters: $\rho_u = 10$ dB, $\rho_p = 20$ dB, $B = 20$ MHz, $B_c = 3$ MHz, $f_c = 2.4$ GHz, and $\tau_{\text{dl}} = \frac{T_{\text{len}}}{8}$.

The numbers of antennas are calculated assuming transmission with a constant bit rate; hence if the drone speed is 20 m/s, the time it takes to transmit each image is 0.8, 2, and 8 seconds, respectively. However, in certain missions (e.g. search and rescue operations), faster transmission might be required. That can be accomplished by increasing the number of antennas beyond the values in Tables I and II. Further, as it can be seen from Figure 9(a), the instantaneous throughput stays at longer time duration due to the similar elevation and azimuth angles of multiple drones. To characterize such events, we have investigated the outage capacity performance of Massive MIMO in LoS conditions in [40]. We have shown that with large number of GS antennas, the outage capacity can be increased as the fluctuations in the interference power becomes negligible due to an interference hardening effect.

In this use case, the total time to complete the mission is $T_{\text{mission}} = \frac{A}{K \cdot v \cdot r_{px} \cdot \text{GSD} \cdot (1 - OL_x)}$ seconds, i.e., K times faster than the single drone case. For $\text{GSD} = 5$ cm, $v = 30$ m/s, $r_{px} \times r_{py} = 2664 \times 1496$, and $OL_x = 60\%$, the mission can be completed within 6 minutes and 16 seconds. On the other hand, a single drone would require more than two hours to complete the mission.

VII. DISCUSSIONS

The proposed Massive MIMO based communication framework could be used for several multi-drone applications that require high throughput communication with high reliability.

TABLE II

DATA RATE REQUIREMENTS FOR COMPRESSED (CR = 200 : 1) VIDEO TRANSMISSION

$r_{py} \times r_{px} \rightarrow$	4096×2160	2664×1496
Q_{video} (60 FPS)	64 Mbps	29 Mbps
$Q_{\text{video}}^{\text{sum}}$ (60 FPS)	1.28 Gbps	580 Mbps
M_{req} (60 FPS)	221	41
M_{req} (30 FPS)	49	15

For example, consider the mission of collecting data from a remote region that is unreachable by humans (e.g. during a search-and-rescue operation or during a natural disaster). The antenna array need not necessarily be located on the ground: One can even think of an aerial network that consists of a master drone (hovering at certain altitude) equipped with an antenna array and a swarm of small UAVs (each equipped with a single antenna) surrounding the master drone.

In practice, the position of the UAVs can have an arbitrary distribution within any arbitrary three-dimensional region. Furthermore, the drones' mobility patterns can be either known a priori, or not. In this work we have selected the random-within-a-sphere mobility model as it facilitates the derivation of certain capacity results in closed form. However, we do not expect that different mobility models would yield significantly different final performance results, as long as the UAVs move fast enough so that each codeword spans over many realizations of the inner products of the spatial signatures. For other distributions of the drone positions, the rate expressions would be similar, but the quantity Ω will be slightly different. This quantity can be interpreted as the correlation between the spatial signatures of the k -th and the j -th UAV. Since Ω is a function of the antenna spacing, optimization of the array geometry is possible. In particular, since the spatial resolvability of an array increases with the element spacing, even if the drones are spatially close to each other, by increasing the antenna spacing one can reduce the correlation between their spatial signatures.

Moreover, from (34) it can be observed that the drone speed has only a slight impact on the pre-log factor and hence on the data rate. For example, consider $\tau_{\text{dl}} = \frac{T_{\text{len}}}{8}$, $B_c = 2$ MHz, $f_c = 5$ GHz and $K = 100$. If we change the UAV speed from $v_{\max} = 0$ m/s to $v_{\max} = 30$ m/s, the change of the pre-log factor is very small, i.e. $0.875 - 0.825 = 0.05$. In (61), the pre-log factor is chosen based on the maximum drone speed – yielding a worst-case design. However, due to the LoS propagation, it may be possible to reduce the frequency of the pilot transmissions. Specifically, if a UAV moves along a trajectory that is known or can be estimated, its channel response may be predicted. This can further boost the payload data rate achieved per drone.

Massive MIMO offers both multiplexing gains and a range extension due to the array gain. In the surveillance use case described above, the distances between the GS and the four corner drones are on the order of several kilometers. Even with a single drone, existing wireless standards cannot support the required range and throughput, and Massive MIMO may be the only feasible solution. In particular, Massive MIMO

technology appears to be much preferable and promising as compared to multi-hop solutions, which are known to suffer from serious drawbacks in terms of reliability and latency [41].

VIII. CONCLUSIONS

Massive MIMO has tremendous potential in the scenario of communication between a ground station and a swarm of drones:

- The multiplexing ability of the array offers huge transmission capacity. See Tables I and II for an example of a drone-swarm surveillance case study, offering sum throughput of 2.4 Gbps (with 2194 antennas) and 1.44 Gbps (with 313 antennas) in 20 MHz bandwidth to 20 drones.
- The array gain of M offers a range extension of a factor \sqrt{M} in line-of-sight. Therefore, the use of Massive MIMO may reduce the need for multi-hop solutions. Alternatively, the array gain can be used to reduce the UAV's transmit power by a factor M .
- Maximal-ratio processing with very low complexity and per-antenna distributed processing is sufficient to obtain very good performance. Additional gains are obtainable through zero-forcing as pointed out in Section IV-B. However, a more detailed study of zero-forcing has to be regarded as future work.
- With (pseudo-) randomly oriented ground station antennas, diversity against polarization mismatches is naturally obtained. This facilitates the use of simple antenna elements, such as cross-dipoles, reducing the concerns of antenna pattern designs.
- If the drones are uniformly distributed inside of a spherical shell, then the optimal antenna spacing is an integer multiple of half a wavelength for a linear array (exactly) and for a rectangular array (approximately).

We hope that the community will reduce our ideas in this paper to practice in the future and perform field trials.

APPENDIX A

APPENDIX A: 3D ROTATION MODEL

A counterclockwise rotation around the reference coordinate axes is described by 1) Roll ($\alpha_x \in [-\frac{\pi}{2}, \frac{\pi}{2}]$): angle of rotation around the x -axis 2) Pitch ($\alpha_y \in [-\frac{\pi}{2}, \frac{\pi}{2}]$): angle of rotation around y -axis 3) Yaw ($\alpha_z \in [0, 2\pi]$): angle of rotation around the z -axis. For example, the transformed unit direction vectors due to a rotation around the x -axis is $(\hat{\mathbf{x}}' \hat{\mathbf{y}}' \hat{\mathbf{z}}') = (\hat{\mathbf{x}} \hat{\mathbf{y}} \hat{\mathbf{z}}) \mathbf{R}_x(\alpha_x)$, where the 3×3 matrix $\mathbf{R}_x(\alpha_x)$ is given by $\mathbf{R}_x(\alpha_x) = \begin{pmatrix} 1 & 0 & 0 \\ 0 & \cos \alpha_x & -\sin \alpha_x \\ 0 & \sin \alpha_x & \cos \alpha_x \end{pmatrix}$. Similarly, the rotation matrices around y - and z -axes are given by $\mathbf{R}_y(\alpha_y) = \begin{pmatrix} \cos \alpha_y & 0 & \sin \alpha_y \\ 0 & 1 & 0 \\ -\sin \alpha_y & 0 & \cos \alpha_y \end{pmatrix}$ and $\mathbf{R}_z(\alpha_z) = \begin{pmatrix} \cos \alpha_z & -\sin \alpha_z & 0 \\ \sin \alpha_z & \cos \alpha_z & 0 \\ 0 & 0 & 1 \end{pmatrix}$, respectively. In practice, the rotation of the UAVs may take place at around any of

the three axes irrespective of the current state of the rotation. In that case, the elements of the rotation matrix depend on the order that the axes are rotated. For example, the rotation matrix that rotates in the order around z -, y -, and x -axes is obtained by $\mathbf{R}(\alpha_z, \alpha_y, \alpha_x) = \mathbf{R}_x(\alpha_x)\mathbf{R}_y(\alpha_y)\mathbf{R}_z(\alpha_z)$.

APPENDIX B: PROOF OF EQUATION (35)

1) *Calculation of $\text{var}(a_2)$:* The variance of the second term of (31) is

$$\text{var}(a_2) = \sum_{j=1, j \neq k}^K \mathbb{E}\{p_{uj}p_{uk}|\hat{\mathbf{g}}_k^H \mathbf{g}_j|^2\}. \quad (68)$$

Let \mathbf{w}_k be the k -th column of \mathbf{W} . Then, $\mathbb{E}\{p_{uj}p_{uk}|\hat{\mathbf{g}}_k^H \mathbf{g}_j|^2\}$ in (68) can be obtained as

$$\begin{aligned} & \mathbb{E}\{p_{uj}p_{uk}|\hat{\mathbf{g}}_k^H \mathbf{g}_j|^2\} \\ &= \mathbb{E}\{p_{uj}p_{uk}\hat{\mathbf{g}}_k^H \mathbf{g}_j \mathbf{g}_j^H \hat{\mathbf{g}}_k\} \\ &= \mathbb{E}\left\{p_{uj}p_{uk}\left(\mathbf{g}_k + \frac{1}{\sqrt{p_p}}\mathbf{w}_k\right)^H \mathbf{g}_j \mathbf{g}_j^H \left(\mathbf{g}_k + \frac{1}{\sqrt{p_p}}\mathbf{w}_k\right)\right\} \\ &= \mathbb{E}\{p_{uj}p_{uk}\mathbf{g}_k^H \mathbf{g}_j \mathbf{g}_j^H \mathbf{g}_k\} \\ &\quad + \frac{1}{\sqrt{p_p}}\mathbb{E}\{\mathbf{g}_k^H\}\mathbb{E}\{p_{uj}p_{uk}\mathbf{g}_j \mathbf{g}_j^H\}\mathbb{E}\{\mathbf{w}_k\} \quad (69) \\ &\quad + \frac{1}{\sqrt{p_p}}\mathbb{E}\{\mathbf{w}_k^H\}\mathbb{E}\{p_{uj}p_{uk}\mathbf{g}_j \mathbf{g}_j^H\}\mathbb{E}\{\mathbf{g}_k\} \\ &\quad + \frac{1}{p_p}\mathbb{E}\{\mathbf{w}_k^H \mathbf{g}_j \mathbf{g}_j^H \mathbf{w}_k\} \\ &= \mathbb{E}\{p_{uj}p_{uk}|\mathbf{g}_k^H \mathbf{g}_j|^2\} + \frac{1}{p_p}\mathbb{E}\{p_{uj}p_{uk}\|\mathbf{g}_j\|^2\} \\ &= \mathbb{E}\{p_{uj}p_{uk}|\mathbf{g}_k^H \mathbf{g}_j|^2\} + \frac{M\rho_u}{p_p}\mathbb{E}\left\{\frac{1}{\beta_k \chi_k}\right\}, \end{aligned}$$

where we used the facts that \mathbf{g}_k and \mathbf{w}_k are independent, $\mathbb{E}\{\mathbf{w}_k\} = \mathbf{0}$, and $\|\mathbf{g}_j\|^2 = M\beta_j \chi_j$.

After substituting (22) and (69) into (68), we get

$$\begin{aligned} \text{var}(a_2) &= \frac{(K-1)M\rho_u}{\rho_p} \chi_{wc} \left(\frac{\lambda}{4\pi d_{wc}} \right)^2 \mathbb{E}\left\{\frac{1}{\beta_k \chi_k}\right\} \quad (70) \\ &\quad + \sum_{j=1, j \neq k}^K \mathbb{E}\{p_{uj}p_{uk}|\mathbf{g}_k^H \mathbf{g}_j|^2\}. \end{aligned}$$

2) *Calculation of $\text{var}(a_1)$:* The variance of the first term of (31) is

$$\begin{aligned} \text{var}(a_1) &= \mathbb{E}\{|p_{uk}\hat{\mathbf{g}}_k^H \mathbf{g}_k - \mathbb{E}\{p_{uk}\hat{\mathbf{g}}_k^H \mathbf{g}_k\}|^2\} \\ &= \mathbb{E}\{p_{uk}^2|\hat{\mathbf{g}}_k^H \mathbf{g}_k|^2\} - |\mathbb{E}\{p_{uk}\hat{\mathbf{g}}_k^H \mathbf{g}_k\}|^2. \quad (71) \end{aligned}$$

From (69), by applying (22) and (28), we get

$$\begin{aligned} \mathbb{E}\{p_{uk}^2|\hat{\mathbf{g}}_k^H \mathbf{g}_k|^2\} &= \mathbb{E}\{p_{uk}^2\|\mathbf{g}_k\|^4\} + \frac{1}{p_p}\mathbb{E}\{p_{uk}^2\|\mathbf{g}_k\|^2\} \\ &= M^2\rho_u^2 + \frac{M\rho_u}{p_p}\mathbb{E}\left\{\frac{1}{\beta_k \chi_k}\right\} \quad (72) \end{aligned}$$

and

$$\begin{aligned} \mathbb{E}\{p_{uk}\hat{\mathbf{g}}_k^H \mathbf{g}_k\} &= \mathbb{E}\left\{p_{uk}\left(\mathbf{g}_k + \frac{1}{\sqrt{p_p}}\mathbf{w}_k\right)^H \mathbf{g}_k\right\} \\ &= \mathbb{E}\{p_{uk}\|\mathbf{g}_k\|^2\} + \frac{1}{\sqrt{p_p}}\mathbb{E}\{\mathbf{w}_k^H\}\mathbb{E}\{p_{uk}\mathbf{g}_k\} \\ &= \mathbb{E}\{p_{uk}\|\mathbf{g}_k\|^2\} \\ &= M\rho_u. \quad (73) \end{aligned}$$

After substituting (72) and (73) into (71), we get

$$\text{var}(a_1) = \frac{M\rho_u}{\rho_p} \chi_{\text{wc}} \left(\frac{\lambda}{4\pi d_{\text{wc}}} \right)^2 \mathbb{E} \left\{ \frac{1}{\beta_k \chi_k} \right\}. \quad (74)$$

3) Calculation of $\text{var}(a_3)$: The variance of the third term of (31) is

$$\begin{aligned} \text{var}(a_3) &= \mathbb{E} \{ p_{uk} \hat{\mathbf{g}}_k^H \mathbf{n} \mathbf{n}^H \hat{\mathbf{g}}_k \} \\ &= \mathbb{E} \{ p_{uk} \mathbf{g}_k^H \mathbf{n} \mathbf{n}^H \mathbf{g}_k \} \\ &\quad + \frac{1}{\sqrt{p_p}} \mathbb{E} \{ p_{uk} \mathbf{g}_k^H \} \mathbb{E} \{ \mathbf{n} \mathbf{n}^H \} \mathbb{E} \{ \mathbf{w}_k \} \\ &\quad + \frac{1}{\sqrt{p_p}} \mathbb{E} \{ \mathbf{w}_k^H \} \mathbb{E} \{ \mathbf{n} \mathbf{n}^H \} \mathbb{E} \{ p_{uk} \mathbf{g}_k \} \\ &\quad + \frac{1}{p_p} \mathbb{E} \{ p_{uk} \mathbf{w}_k^H \mathbf{n} \mathbf{n}^H \mathbf{w}_k \} \\ &= M\rho_u + \frac{M}{\rho_p} \chi_{\text{wc}} \left(\frac{\lambda}{4\pi d_{\text{wc}}} \right)^2 \mathbb{E} \left\{ \frac{1}{\beta_k \chi_k} \right\}. \end{aligned} \quad (75)$$

After substituting (70), (73), (74), and (75) into (33), we get (35).

Here

$$\begin{aligned} \mathbb{E} \{ \cos(b_{ll'} / d_k) \} &= \int_{R_{\min}}^R \cos \left(\frac{b_{ll'}}{r} \right) f_{d_k}(r) dr \\ &= \int_{R_{\min}}^R \cos \left(\frac{b_{ll'}}{r} \right) \frac{3r^2}{R^3 - R_{\min}^3} dr \\ &= \frac{1}{R^3 - R_{\min}^3} \left(r^3 \cos \left(\frac{b_{ll'}}{r} \right) \Big|_{R_{\min}}^R - \int_{R_{\min}}^R r^3 d \cos \left(\frac{b_{ll'}}{r} \right) \right) \\ &= \frac{1}{R^3 - R_{\min}^3} \left(r^3 \cos \left(\frac{b_{ll'}}{r} \right) \Big|_{R_{\min}}^R - b_{ll'} \int_{R_{\min}}^R r \sin \left(\frac{b_{ll'}}{r} \right) dr \right) \\ &= \frac{1}{R^3 - R_{\min}^3} \left(r^3 \cos \left(\frac{b_{ll'}}{r} \right) \Big|_{R_{\min}}^R \right. \\ &\quad \left. - \frac{b_{ll'}}{2} \left(r^2 \sin \left(\frac{b_{ll'}}{r} \right) \Big|_{R_{\min}}^R + b_{ll'} \int_{R_{\min}}^R \cos \left(\frac{b_{ll'}}{r} \right) dr \right) \right) \\ &= \frac{1}{R^3 - R_{\min}^3} \left(r^3 \cos \left(\frac{b_{ll'}}{r} \right) \Big|_{R_{\min}}^R - \frac{b_{ll'}}{2} r^2 \sin \left(\frac{b_{ll'}}{r} \right) \Big|_{R_{\min}}^R \right. \\ &\quad \left. - \frac{b_{ll'}^2}{2} \left(r \cos \left(\frac{b_{ll'}}{r} \right) \Big|_{R_{\min}}^R - b_{ll'} \int_{R_{\min}}^R \frac{\sin \left(\frac{b_{ll'}}{r} \right)}{r} dr \right) \right) \\ &= \frac{1}{2(R^3 - R_{\min}^3)} \left((2r^2 - b_{ll'}^2)r \cos \left(\frac{b_{ll'}}{r} \right) \Big|_{R_{\min}}^R \right. \\ &\quad \left. - b_{ll'} r^2 \sin \left(\frac{b_{ll'}}{r} \right) \Big|_{R_{\min}}^R - b_{ll'}^3 \int_{R_{\min}}^R \frac{\sin \left(\frac{b_{ll'}}{r} \right)}{r} dr \right). \end{aligned} \quad (77)$$

The last integral in (77) can be calculated as

APPENDIX C

APPENDIX C: PROOF OF EQUATIONS (49) AND (50)

4) Proof of Equation (49): By letting

$$\begin{aligned} \int_{R_{\min}}^R \frac{\sin \left(\frac{b_{ll'}}{r} \right)}{r} dr &= - \int_{(b_{ll'})/R_{\min}}^{b_{ll'}/R} \frac{\sin(t)}{t} dt \\ &= -\text{Si}(b_{ll'}/r) \Big|_{R_{\min}}^R \\ &= \text{Si}(b_{ll'}/R) - \text{Si}(b_{ll'}/R_{\min}), \end{aligned} \quad (78)$$

$$b_{ll'} = \frac{\pi}{\lambda} ((p-1)^2 - (p'-1)^2) \delta_x^2 + ((q-1)^2 - (q'-1)^2) \delta_y^2,$$

where $\text{Si}(x) = \int_0^x \frac{\sin t}{t} dt$. By substituting (78) into (77), we get

Equation (49) can be written as

$$\begin{aligned} \mathbb{E} \left\{ e^{i \frac{\pi}{\lambda} \frac{1}{d_k} [(p-1)^2 - (p'-1)^2] \delta_x^2 + ((q-1)^2 - (q'-1)^2) \delta_y^2} \right\} \\ = \mathbb{E} \left\{ e^{i \frac{b_{ll'}}{d_k}} \right\} \\ = \mathbb{E} \{ \cos(b_{ll'}/d_k) \} + i \mathbb{E} \{ \sin(b_{ll'}/d_k) \}. \end{aligned} \quad (76)$$

$$\begin{aligned} \mathbb{E} \{ \cos(b_{ll'}/d_k) \} \\ = \frac{1}{2(R^3 - R_{\min}^3)} \\ \times \left((2R^2 - b_{ll'}^2) R \cos(b_{ll'}/R) - b_{ll'} R^2 \sin(b_{ll'}/R) \right. \\ \left. + b_{ll'}^3 \text{Si}(b_{ll'}/R) - (2R_{\min}^2 - b_{ll'}^2) R_{\min} \cos(b_{ll'}/R_{\min}) \right. \\ \left. + b_{ll'} R_{\min}^2 \sin(b_{ll'}/R_{\min}) - b_{ll'}^3 \text{Si}(b_{ll'}/R_{\min}) \right). \end{aligned}$$

Similarly,

$$\begin{aligned} \mathbb{E}\{\sin(b_{ll'}/d_k)\} &= \frac{1}{2(R^3 - R_{\min}^3)} \\ &\times \left((2R^2 - b_{ll'}^2)R \sin(b_{ll'}/R) + b_{ll'}R^2 \cos(b_{ll'}/R) \right. \\ &+ b_{ll'}^3 \text{Ci}(b_{ll'}/R) - (2R_{\min}^2 - b_{ll'}^2)R_{\min} \sin(b_{ll'}/R_{\min}) \\ &\left. - b_{ll'}R_{\min}^2 \cos(b_{ll'}/R_{\min}) - b_{ll'}^3 \text{Ci}(b_{ll'}/R_{\min}) \right), \end{aligned}$$

where $\text{Ci}(x) = -\int_x^\infty \frac{\cos t}{t} dt$. Now by letting $\mathbb{C}(b_{ll'}) = \mathbb{E}\{\cos(b_{ll'}/d_k)\}$ and $\mathbb{D}(b_{ll'}) = \mathbb{E}\{\sin(b_{ll'}/d_k)\}$, the expectation in (76) is expressed as given in (49).

5) Proof of Equation (50):

$$\begin{aligned} \mathbb{E}\left\{e^{i\frac{2\pi}{\lambda}((p-p')\delta_x \sin \theta_k \cos \phi_k + (q-q')\delta_y \sin \theta_k \sin \phi_k)}\right\} &= \int_0^{2\pi} \int_0^\pi e^{i\frac{2\pi}{\lambda}((p-p')\delta_x \sin \theta \cos \phi + (q-q')\delta_y \sin \theta \sin \phi)} \\ &\quad \times f_{\theta_k}(\theta) f_{\phi_k}(\phi) d\theta d\phi \\ &= \frac{1}{4\pi} \int_0^{2\pi} \int_0^\pi e^{i\frac{2\pi}{\lambda}((p-p')\delta_x \sin \theta \cos \phi + (q-q')\delta_y \sin \theta \sin \phi)} \sin \theta d\theta d\phi. \end{aligned}$$

By letting $\alpha_1 = \frac{(p-p')\delta_x}{\lambda}$ and $\alpha_2 = \frac{(q-q')\delta_y}{\lambda}$, the above integral can be rewritten as

$$\frac{1}{4\pi} \int_0^{2\pi} \int_0^\pi e^{i2\pi(\alpha_1 \sin x \cos y + \alpha_2 \sin x \sin y)} \sin x dxdy.$$

First we observe that $\alpha_1 \cos y + \alpha_2 \sin y = \sqrt{\alpha_1^2 + \alpha_2^2} \left(\frac{\alpha_1}{\sqrt{\alpha_1^2 + \alpha_2^2}} \cos y + \frac{\alpha_2}{\sqrt{\alpha_1^2 + \alpha_2^2}} \sin y \right)$ and we can find an angle $\xi \in [0, 2\pi)$, such that $\cos \xi = \frac{\alpha_1}{\sqrt{\alpha_1^2 + \alpha_2^2}}$ and $\sin \xi = \frac{\alpha_2}{\sqrt{\alpha_1^2 + \alpha_2^2}}$. Thus we can simplify the expression as $\alpha_1 \cos y + \alpha_2 \sin y = \sqrt{\alpha_1^2 + \alpha_2^2} (\cos \xi \cos y + \sin \xi \sin y) = \sqrt{\alpha_1^2 + \alpha_2^2} \cos(y - \xi)$, which leads to

$$\begin{aligned} \frac{1}{4\pi} \int_0^{2\pi} \int_0^\pi e^{i2\pi(\alpha_1 \cos y + \alpha_2 \sin y)} \sin x dxdy &= \frac{1}{4\pi} \int_0^{2\pi} \int_0^\pi e^{i2\pi \alpha \sin x \cos(y - \xi)} \sin x dxdy \\ &= \frac{1}{4\pi} \int_0^{2\pi} \int_0^\pi e^{i2\pi \alpha \sin x \cos y} \sin x dxdy, \end{aligned} \quad (79)$$

where $\alpha = \sqrt{\alpha_1^2 + \alpha_2^2}$. By applying the following symmetries of the trigonometric functions $\cos y = \cos(2\pi - y)$, $\sin x = \sin(\pi - x)$ and $\cos y = -\cos(\pi - y)$ we

consecutively calculate

$$\begin{aligned} \frac{1}{4\pi} \int_0^{2\pi} \int_0^\pi e^{i2\pi \alpha \sin x \cos y} \sin x dxdy &= \frac{1}{2\pi} \int_0^\pi \int_0^\pi e^{i2\pi \alpha \sin x \cos y} \sin x dxdy \\ &= \frac{1}{\pi} \int_0^\pi \int_0^{\frac{\pi}{2}} e^{i2\pi \alpha \sin x \cos y} \sin x dxdy \\ &= \frac{1}{\pi} \left(\int_0^{\frac{\pi}{2}} \int_0^{\frac{\pi}{2}} e^{i2\pi \alpha \sin x \cos y} \sin x dxdy \right. \\ &\quad \left. + \int_0^{\frac{\pi}{2}} \int_0^{\frac{\pi}{2}} e^{-i2\pi \alpha \sin x \cos y} \sin x dxdy \right). \end{aligned} \quad (80)$$

By defining the function

$$h(\alpha) = \int_0^{\frac{\pi}{2}} \int_0^{\frac{\pi}{2}} e^{i2\pi \alpha \sin x \cos y} \sin x dxdy$$

and using (80), we get

$$\begin{aligned} \frac{1}{4\pi} \int_0^{2\pi} \int_0^\pi e^{i2\pi \alpha \sin x \cos y} \sin x dxdy &= \frac{1}{\pi} (h(\alpha) + h^*(\alpha)) \\ &= \frac{2}{\pi} \Re\{h(\alpha)\}. \end{aligned} \quad (81)$$

We calculate the Fourier transform of $h(\alpha)$ as

$$\begin{aligned} H(f) = \mathcal{F}\{h(\alpha)\} &= \int_{-\infty}^{\infty} h(\alpha) e^{-i2\pi \alpha f} d\alpha \\ &= \int_{-\infty}^{\infty} \int_0^{\frac{\pi}{2}} \int_0^{\frac{\pi}{2}} e^{i2\pi \alpha \sin x \cos y} \sin x dxdy e^{-i2\pi \alpha f} d\alpha \\ &= \int_0^{\frac{\pi}{2}} \int_0^{\frac{\pi}{2}} \left(\int_{-\infty}^{\infty} e^{-i2\pi \alpha(f - \sin x \cos y)} d\alpha \right) \sin x dxdy \\ &= \int_0^{\frac{\pi}{2}} \int_0^{\frac{\pi}{2}} \delta(f - \sin x \cos y) \sin x dxdy \\ &= \begin{cases} \int_0^{\frac{\pi}{2}} \int_0^{\frac{\pi}{2}} \delta(f - \sin x \cos y) \sin x dxdy, & \text{if } f \in [0, 1], \\ 0, & \text{if } f \notin [0, 1]. \end{cases} \end{aligned} \quad (82)$$

Here we used the facts that $\sin x \cos y \in [0, 1]$ when $x, y \in [0, \frac{\pi}{2}]$ and that

$$\int_A f(x) \delta(g(x)) dx = \sum_i \frac{f(x_i)}{|g'(x_i)|}, \quad (83)$$

where $x_i \in A \subseteq \mathbb{R}$ are all roots of $g(x)$ (i.e. $g(x_i) = 0$) in the set A . If $g(x)$ has no roots in A , then the integral in (83) is equal to zero. We proceed with the calculation of the inner integral in (82). We observe that in this case we have $f \in [0, 1]$, $\sin x \in [0, 1]$ and $\cos y \in [0, 1]$. Using (83) we can conclude that

$$\begin{aligned} \int_0^{\frac{\pi}{2}} \delta(f - \sin x \cos y) \sin x dx &= \begin{cases} \frac{\sin(\arcsin(\frac{f}{\cos y}))}{|-\cos(\arcsin(\frac{f}{\cos y})) \cos y|}, & \text{if } f \in [0, \cos y], \\ 0, & \text{if } f \in (\cos y, 1] \end{cases} \\ &= \begin{cases} \frac{f}{\cos y \sqrt{\cos^2 y - f^2}}, & \text{if } y \in [0, \arccos f], \\ 0, & \text{if } y \in (\arccos f, \frac{\pi}{2}]. \end{cases} \end{aligned} \quad (84)$$

Now we can calculate the double integral in (82) by applying several variable changes. Inserting (84) in (82) we obtain

$$\begin{aligned}
& \int_0^{\frac{\pi}{2}} \int_0^{\frac{\pi}{2}} \delta(f - \sin x \cos y) \sin x \, dx dy \\
&= \int_0^{\arccos f} \frac{f}{\cos y \sqrt{\cos^2 y - f^2}} \, dy \quad /y = \arcsin t/ \\
&= \int_0^{\sqrt{1-f^2}} \frac{f}{(1-t^2)\sqrt{1-t^2-f^2}} \, dt \quad /t=(p-p')\sqrt{1-f^2}/ \\
&= \int_0^1 \frac{f}{(1-(p-p')^2(1-f^2))\sqrt{1-(p-p')^2}} \, du \\
&\quad /p-p'=\cos t/ \tag{85} \\
&= \int_0^{\frac{\pi}{2}} \frac{f}{\sin^2 t + f^2 \cos^2 t} \, dt \\
&= \int_0^{\frac{\pi}{2}} \frac{2f}{(f^2+1)+(f^2-1)\cos 2t} \, dt \quad /t=\frac{\pi-2u}{4}/ \\
&= \int_{-\frac{\pi}{2}}^{\frac{\pi}{2}} \frac{f}{(f^2+1)+(f^2-1)\sin(p-p')} \, du \\
&= \frac{f}{2f} \arcsin \left(\frac{(f^2+1)\sin(p-p')+(f^2-1)}{(f^2+1)+(f^2-1)\sin(p-p')} \right) \Big|_{-\frac{\pi}{2}}^{\frac{\pi}{2}} \\
&= \frac{\pi}{2}.
\end{aligned}$$

Combining (82) and (85) we get

$$H(f) = \frac{\pi}{2} \operatorname{rect}\left(f - \frac{1}{2}\right) = \begin{cases} \frac{\pi}{2}, & \text{if } f \in [0, 1], \\ 0, & \text{if } f \notin [0, 1], \end{cases}$$

where the rectangular pulse function is defined as

$$\operatorname{rect}(t) = \begin{cases} 1, & \text{if } t \in \left[-\frac{1}{2}, \frac{1}{2}\right], \\ 0, & \text{if } t \notin \left[-\frac{1}{2}, \frac{1}{2}\right]. \end{cases}$$

The function $h(\alpha)$ can be derived by taking the inverse Fourier transform $H(f)$ as follows

$$\begin{aligned}
h(\alpha) &= \mathcal{F}^{-1}\{H(f)\} = \frac{\pi}{2} \mathcal{F}^{-1}\left\{\operatorname{rect}\left(f - \frac{1}{2}\right)\right\} \\
&= \frac{\pi}{2} e^{i2\pi\frac{1}{2}\alpha} \mathcal{F}^{-1}\{\operatorname{rect}(f)\} = \frac{\pi}{2} e^{i\pi\alpha} \operatorname{sinc}(\alpha). \tag{86}
\end{aligned}$$

Using (79), (81), and (86), the original integral can be obtained as

$$\begin{aligned}
& \frac{1}{4\pi} \int_0^{2\pi} \int_0^\pi e^{i2\pi \sin x (\alpha_1 \cos y + \alpha_2 \sin y)} \sin x \, dx dy \\
&= \frac{2}{\pi} \Re\{h(\alpha)\} = \frac{2}{\pi} \frac{\pi}{2} \Re\{e^{i\pi\alpha}\} \operatorname{sinc}(\alpha) \\
&= \cos(\pi\alpha) \operatorname{sinc}(\alpha) = \frac{\cos(\pi\alpha) \sin(\pi\alpha)}{\pi\alpha} \\
&= \frac{\sin(2\pi\alpha)}{2\pi\alpha} = \operatorname{sinc}(2\alpha). \tag{87}
\end{aligned}$$

Finally, by substituting α_1 , α_2 , and α , we get

$$\begin{aligned}
& \mathbb{E}\left\{e^{i\frac{2\pi}{\lambda}((p-p')\delta_x \sin \theta_k \cos \phi_k + (q-q')\delta_y \sin \theta_k \sin \phi_k)}\right\} \\
&= \operatorname{sinc}\left(\frac{2}{\lambda} \sqrt{(p-p')^2 \delta_x^2 + (q-q')^2 \delta_y^2}\right).
\end{aligned}$$

REFERENCES

- [1] P. Chandhar, D. Danev, and E. G. Larsson, "Massive MIMO as enabler for communications with drone swarms," in *Proc. International Conference on Unmanned Aircraft Systems (ICUAS)*, June 2016, pp. 347–354.
- [2] ———, "On ergodic rates and optimal array geometry in line-of-sight Massive MIMO," in *Proc. IEEE SPAWC*, July 2016, pp. 1–6.
- [3] S. Hayat, E. Yanmaz, and R. Muzaffar, "Survey on unmanned aerial vehicle networks for civil applications: A communications viewpoint," *IEEE Commun. Surveys Tuts.*, vol. 18, no. 4, pp. 2624–2661, Fourth-Quarter 2016.
- [4] L. Gupta, R. Jain, and G. Vaszkun, "Survey of important issues in UAV communication networks," *IEEE Commun. Surveys Tuts.*, vol. 18, no. 2, pp. 1123–1152, Second-Quarter 2016.
- [5] M. Asadpour, B. Van den Bergh, D. Giustiniano, K. Hummel, S. Pollin, and B. Plattner, "Micro aerial vehicle networks: An experimental analysis of challenges and opportunities," *IEEE Commun. Mag.*, vol. 52, no. 7, pp. 141–149, July 2014.
- [6] T. Andre, K. Hummel, A. Schoellig, E. Yanmaz, M. Asadpour, C. Bettstetter, P. Grippa, H. Hellwagner, S. Sand, and S. Zhang, "Application-driven design of aerial communication networks," *IEEE Commun. Mag.*, vol. 52, no. 5, pp. 129–137, May 2014.
- [7] E. Yanmaz, R. Kuschnig, and C. Bettstetter, "Achieving air-ground communications in 802.11 networks with three-dimensional aerial mobility," in *Proc. IEEE INFOCOM*, Apr. 2013, pp. 120–124.
- [8] M. Asadpour, K. A. Hummel, D. Giustiniano, and S. Draskovic, "Route or carry: Motion-driven packet forwarding in micro aerial vehicle networks," *IEEE Trans. Mobile Comput.*, vol. 16, no. 3, pp. 843–856, Mar. 2017.
- [9] M. Asadpour, D. Giustiniano, K. A. Hummel, S. Heimlicher, and S. Egli, "Now or later?: Delaying data transfer in time-critical aerial communication," in *Proc. ACM Conference on Emerging Networking Experiments and Technologies CoNEXT*, 2013, pp. 127–132.
- [10] S. Hayat, E. Yanmaz, and C. Bettstetter, "Experimental analysis of multipoint-to-point UAV communications with IEEE 802.11n and 802.11ac," in *Proc. IEEE PIMRC*, Aug. 2015, pp. 1991–1996.
- [11] Abatti J., *Small Power: The Role of Micro and Small UAVs in the Future*. Maxwell AFB, AL: Air Command and Staff College, 2005.
- [12] P. Olsson, J. Kvarnstrom, P. Doherty, O. Burdakov, and K. Holmberg, "Generating UAV communication networks for monitoring and surveillance," in *Proc. International Conference on Control Automation Robotics Vision (ICARCV)*, Dec. 2010, pp. 1070–1077.
- [13] T. L. Marzetta, E. G. Larsson, H. Yang, and H. Q. Ngo, *Fundamentals of Massive MIMO*. Cambridge University Press, 2016.
- [14] T. Marzetta, "Noncooperative cellular wireless with unlimited numbers of base station antennas," *IEEE Trans. Wireless Commun.*, vol. 9, no. 11, pp. 3590–3600, Nov. 2010.
- [15] E. G. Larsson, O. Edfors, F. Tufvesson, and T. Marzetta, "Massive MIMO for next generation wireless systems," *IEEE Commun. Mag.*, vol. 52, no. 2, pp. 186–195, Feb. 2014.
- [16] J. Rasool, G. Oien, J. Hakegard, and T. Myrvoll, "On multiuser MIMO capacity benefits in air-to-ground communication for air traffic management," in *Proc. ISWCS*, Sept. 2009, pp. 458–462.
- [17] Y. Jiang, A. Tiwari, M. Rachid, and B. Daneshrad, "MIMO for airborne communications [industry perspectives]," *IEEE Wireless Commun. Mag.*, vol. 21, no. 5, pp. 4–6, Oct. 2014.
- [18] W. Su, J. D. Matijas, M. J. Gans, and S. Batalama, "Maximum achievable capacity in airborne MIMO communications with arbitrary alignments of linear transceiver antenna arrays," *IEEE Trans. Wireless Commun.*, vol. 12, no. 11, pp. 5584–5593, Nov. 2013.
- [19] E. T. Michailidis and A. G. Kanatas, "Three-dimensional HAP-MIMO channels: Modeling and analysis of space-time correlation," *IEEE Trans. Veh. Technol.*, vol. 59, no. 5, pp. 2232–2242, June 2010.
- [20] I. Sarris and A. Nix, "Maximum MIMO capacity in line-of-sight," in *Proc. International Conference on Information, Communications and Signal Processing*, Dec. 2005, pp. 1236–1240.
- [21] F. Bohagen, P. Orten, and G. Oien, "Design of optimal high-rank line-of-sight MIMO channels," *IEEE Trans. Wireless Commun.*, vol. 6, no. 4, pp. 1420–1425, Apr. 2007.
- [22] T. Halsig and B. Lankl, "Array size reduction for high-rank LoS MIMO ULAs," *IEEE Microw. Wireless Compon. Lett.*, vol. 4, no. 6, pp. 649–652, Dec. 2015.
- [23] J. Chen, "When does asymptotic orthogonality exist for very large arrays?" in *Proc. IEEE GLOBECOM*, Dec. 2013, pp. 4146–4150.
- [24] Y. Hu, Y. Hong, and J. Evans, "Interference in LoS Massive MIMO is well approximated by a Beta-mixture," in *Proc. IEEE ICC Workshops*, June 2015, pp. 1137–1142.

- [25] W. Tan, S. Jin, J. Wang, and Y. Huang, "Achievable sum-rate analysis for Massive MIMO systems with different array configurations," in *Proc. IEEE WCNC*, Mar. 2015, pp. 316–321.
- [26] H. Yang and T. L. Marzetta, "Massive MIMO with max-min power control in line-of-sight propagation environment," *IEEE Transactions on Communications*, vol. 65, no. 11, pp. 4685–4693, Nov. 2017.
- [27] M. Shafi, M. Zhang, A. Moustakas, P. Smith, A. Molisch, F. Tufvesson, and S. Simon, "Polarized MIMO channels in 3-D: Models, measurements and mutual information," *IEEE J. Select. Areas Commun.*, vol. 24, no. 3, pp. 514–527, Mar. 2006.
- [28] M.-T. Dao, V.-A. Nguyen, Y.-T. Im, S.-O. Park, and G. Yoon, "3D polarized channel modeling and performance comparison of MIMO antenna configurations with different polarizations," *IEEE Trans. Antennas Propag.*, vol. 59, no. 7, pp. 2672–2682, July 2011.
- [29] S. Jaekel, K. Borner, L. Thiele, and V. Jungnickel, "A geometric polarization rotation model for the 3-D spatial channel model," *IEEE Trans. Antennas Propag.*, vol. 60, no. 12, pp. 5966–5977, Dec. 2012.
- [30] C. A. Balanis, *Antenna Theory: Analysis and Design*. Wiley-Interscience, 2005.
- [31] R. Sun, D. W. Matolak, and W. Rayess, "Air-ground channel characterization for unmanned aircraft systems—Part IV: Airframe shadowing," *IEEE Trans. Veh. Technol.*, vol. 66, no. 9, pp. 7643–7652, Sept. 2017.
- [32] D. W. Matolak and R. Sun, "Air-ground channel characterization for unmanned aircraft systems—Part I: Methods, measurements, and models for over-water settings," *IEEE Trans. Veh. Technol.*, vol. 66, no. 1, pp. 26–44, Jan. 2017.
- [33] R. Sun and D. W. Matolak, "Air-ground channel characterization for unmanned aircraft systems—Part II: Hilly and mountainous settings," *IEEE Trans. Veh. Technol.*, vol. 66, no. 3, pp. 1913–1925, Mar. 2017.
- [34] D. W. Matolak and R. Sun, "Air-ground channel characterization for unmanned aircraft systems—Part III: The suburban and near-urban environments," *IEEE Trans. Veh. Technol.*, vol. 66, no. 8, pp. 6607–6618, Aug. 2017.
- [35] Rappaport T. S., *Wireless Communications Principles and Practice*. Prentice Hall Inc., 1996.
- [36] P. D. Teal, T. D. Abhayapala, and R. A. Kennedy, "Spatial correlation for general distributions of scatterers," *IEEE Signal Process. Lett.*, vol. 9, no. 10, pp. 305–308, Oct. 2002.
- [37] D. E. Knuth, *The Art of Computer Programming, Volume 2 (3rd Ed.): Seminumerical Algorithms*. Boston, MA, USA: Addison-Wesley Longman Publishing Co., Inc., 1997.
- [38] "Drones and aerial observation: New technologies for property rights, human rights, and global development - A primer," <http://drones.newamerica.org/primer/DronesAndAerialObservation.pdf>, [Online], Accessed: May 15, 2018.
- [39] T. Rosnell and E. Honkavaara, "Point cloud generation from aerial image data acquired by a quadrocopter type micro unmanned aerial vehicle and a digital still camera," *Sensors*, vol. 12, no. 1, pp. 453–480, Jan. 2012.
- [40] P. Chandhar, D. Danev, and E. G. Larsson, "On the outage capacity in Massive MIMO with line-of-sight," in *Proc. IEEE SPAWC*, July 2017, pp. 1–6.
- [41] L. R. Pinto, L. Almeida, and A. Rowe, "Demo abstract: Video streaming in multi-hop aerial networks," in *Proc. ACM/IEEE International Conference on Information Processing in Sensor Networks*, Apr. 2017, pp. 283–284.



Prabhu Chandhar received the Ph.D. Degree from Indian Institute of Technology Kharagpur, West Bengal, India. From Nov. 2015 to Oct. 2017, he was a Postdoctoral Researcher at the Division of Communication Systems, Linköping University (LiU), Linköping, Sweden. From Aug. 2009 to July 2010, he worked as a Senior Research Fellow at Vodafone IIT KGP Centre of Excellence in Telecommunications (VICET), IIT Kharagpur, India. His research interests are within the fields of signal processing and communication theory.



Danyo Danev received his MSc in mathematics from Sofia University in 1996 and his PhD in electrical engineering from Linköping University in 2001. In 2005 he obtained Docent title in Data Transmission. He is currently Associate Professor at Linköping University, Sweden. His research interests are within the fields of coding, information and communication theory. He has authored or co-authored 2 book chapters, 17 journal papers and more than 30 conference papers on these topics. He is currently teaching a number of communication engineering and mathematics courses. Since 2012 he is board member of the IEEE Sweden VT/COM/IT Chapter.



Erik G. Larsson received the Ph.D. degree from Uppsala University, Uppsala, Sweden, in 2002. He is currently Professor of Communication Systems at Linköping University (LiU) in Linköping, Sweden. He was with the Royal Institute of Technology (KTH) in Stockholm, Sweden, the University of Florida, USA, the George Washington University, USA, and Ericsson Research, Sweden. In 2015 he was a Visiting Fellow at Princeton University, USA, for four months. His main professional interests are within the areas of wireless communications and signal processing. He has co-authored some 130 journal papers on these topics, he is co-author of the two Cambridge University Press textbooks *Space-Time Block Coding for Wireless Communications* (2003) and *Fundamentals of Massive MIMO* (2016). He is co-inventor on 16 issued and many pending patents on wireless technology.

He was Associate Editor for, among others, the *IEEE Transactions on Communications* (2010–2014) and the *IEEE Transactions on Signal Processing* (2006–2010). From 2015 to 2016 he served as chair of the IEEE Signal Processing Society SPCOM technical committee, and in 2017 he is the past chair of this committee. From 2014 to 2015 he served as chair of the steering committee for the *IEEE Wireless Communications Letters*. He was the General Chair of the Asilomar Conference on Signals, Systems and Computers in 2015, and its Technical Chair in 2012. He is a member of the IEEE Signal Processing Society Awards Board during 2017–2019.

He received the IEEE Signal Processing Magazine Best Column Award twice, in 2012 and 2014, the IEEE ComSoc Stephen O. Rice Prize in Communications Theory in 2015, and the IEEE ComSoc Leonard G. Abraham Prize in 2017. He is a Fellow of the IEEE.